Impact of topography on earthquake static slip estimates

Leah Langer[a,**], Théa Ragon[b,c,**], Anthony Sladen[b], Jeroen Tromp[a,d]

[a]*Department of Geosciences, Princeton University, USA*
[b]*Université Côte d'Azur, CNRS, IRD, OCA, Géoazur, 250 rue Albert Einstein, 06560 Valbonne, France*
[c]*Seismological Laboratory, California Institute of Technology, 1200 E. California Blvd., Pasadena, CA 91125, USA*
[d]*Program in Applied & Computational Mathematics, Princeton University, USA*

Abstract

Our understanding of earthquakes is limited by our knowledge, and our description, of the physics of the Earth. When solving for subsurface fault slip, it is common practice to assume minimum complexity for characteristics such as topography, fault geometry and elastic properties. These characteristics are rarely accounted for because our knowledge of them is often partial and they can be difficult to include in simulations. However, topography and bathymetry are known all over the Earth's surface, and recently developed software packages such as SPECFEM-X have simplified the process of including them in calculations. Here, we explore the impact of topography on static slip estimates. We also investigate whether the influence of topography can be accounted for with a zeroth-order correction which accounts for variations in distance between subfaults and the surface of the domain. To this end, we analyze the 2015 M_w 7.5 Gorkha, Nepal, and the 2010 M_w 8.8 Maule, Chile, earthquakes within a Bayesian framework. The regions affected by these events represent different types of topography. Chile, which contains both a deep trench and a major orogen, the Andes, has a greater overall elevation range and steeper gradients than Nepal, where the primary topographic feature is the Himalayan mountain range. Additionally, the slip of the continental Nepal event is well-constrained, whereas observations are less informative in a subduction context. We show that topography has a non-negligible impact on inferred slip models. Our results suggest that the effect of topography on slip estimates increases with limited observational constraints and high elevation gradients. In particular, we find that accounting for topography improves slip estimates where topographic gradients are large. When topography has a significant impact on slip, the zeroth-order correction is not sufficient.

Keywords: Earthquake source observations, Inverse theory, Probability distributions,

---

[*]Equally contributing author, corresponding author
[**]Equally contributing author, corresponding author
   Email addresses: `llanger@princeton.edu` (Leah Langer), `tragon@caltech.edu` (Théa Ragon)

1. Introduction

Estimates of subsurface fault slip are mainly constrained by observations of earthquake-induced deformation on the surface of the Earth, but they are also sensitive to information specified a priori to characterize the forward model. The forward model will always be an approximation to the real Earth, and these approximations can affect inferences of fault slip (e.g., Beresnev, 2003; Hartzell et al., 2007). We often assume minimum complexity for the forward problem, partly because we are not certain about many detailed aspects of Earth structure, but also to simplify Green's functions computations. The simplest, and commonly used, description of the forward problem is a planar fault in a homogeneous elastic half-space with a flat surface. It is true that certain characteristics of the forward model, such as fault geometry and elastic heterogeneity, are often poorly known, but topography and bathymetry are well-constrained at the global scale.

In previous studies, synthetic tests have shown that topography of the free surface, within a simple configuration, can have a significant impact on predicted static surface deformation, particularly if the source is located at shallow depths (e.g., McTigue and Segall, 1988; Huang and Yeh, 1997; Williams and Wadge, 1998; Tinti and Armigliato, 2002). Within a realistic setup, several studies have found that Green's functions produced with a 3D model which includes topography and 3D elastic structure yield more accurate sub-surface fault slip estimates (e.g., Zhao et al., 2004; Moreno et al., 2012; Kyriakopoulos et al., 2013; Gallovič et al., 2015; Tung and Masterlark, 2016; Wang et al., 2017; Wang and Fialko, 2018). However, because most of these studies did not separate the effects of topography from those of heterogeneous elastic structure, it is not possible to determine the impact of topography alone from their results.

A few studies did examine the effect of topography on predicted surface deformation or estimated sub-surface fault slip. Most of those studies analyzed earthquakes in regions with relatively small topographic gradients, so the effects of topography were not found to be significant. Masterlark (2003) suggested that the effect of topography on both predicted surface displacements and inferred slip, within a subduction context, is negligible when compared to the impact of elastic heterogeneity. However, the earthquake used in that study was the 1995 M_w 8.0 Jalisco-Colisma earthquake in Mexico, where the topography gradient is of limited amplitude and confined near the trench. Similarly, Trasatti et al. (2011) showed that the addition of topography had a minimal effect on the slip distribution of the 2009 M_w 6.3 L'Aquila event in Italy due to the lack of strong topographic variations in the region. Williams and Wallace (2018) investigated shallow slow slip

at the Hikurangi Subduction Margin in New Zealand, where the topographic gradient is relatively smooth. They determined that accounting for topography would only yielded a slight variation in their slip models (5% difference in seismic potency), which is much smaller than the effect they found for crustal heterogeneity (>50% difference in seismic potency). In contrast, Hsu et al. (2011) did examine the impact of topography on the predicted surface displacement for an earthquake that occurred in a region with significant topographic variations: the 2005 M_w 8.7 Sumatra subduction event. They demonstrated than the effect of topography on predicted surface deformation can be significant, especially if the fault slip occurs close to areas with strong topographic gradients.

Most studies that included topographic structure used finite-element (or other numerical) methods to calculate Green's functions for quasi-static deformation. In some settings, it is possible to calculate these Green's functions semi-analytically. Williams and Wadge (2000) developed a semi-analytical method for calculating deformation in a region with topography via a first-order perturbation to the elastic half-space solution. This first-order correction accounts for both aspects of the topographic effect: topography-induced variations in distance between the fault and the surface of the domain, and the elastic effect caused by the shape of the topographic surface. However, this solution is only valid when topographic gradients are mild, and cannot be used in settings with extreme topography. Numerical simulation methods are required to produce Green's functions in those settings.

A previous study by some of these authors, Langer et al. (2019), found that the inclusion of topography has a significant effect on predicted surface deformation in a variety of settings. In particular, they modeled the 2015 Gorkha earthquake and found that 3D elastic structure and topography each caused differences of 10% in predicted coseismic surface deformation. However, the differences due to topography were more significant because they affected the shape of the deformation pattern, not only its magnitude. In this study, we seek to build on those results by investigating the extent to which those differences in the predicted surface displacement pattern are mapped onto the inferred slip distribution.

Although previous studies have made some progress in investigating the impact of Green's functions with 3D structure on coseismic slip models, the effects of topography have not been thoroughly examined. Topography is very well known for every region in the world, and thus above any earthquake rupture, and yet its influence remains poorly investigated. Accounting for topography is a simple way to include accurate information about the Earth in our inverse problem. We wish to know whether the inclusion of topography is necessary to infer accurate results in regions with topographic variations, and whether neglecting topography can impact our estimates of slip distribution.

An additional question that we wish to investigate is whether Green's functions with a zeroth-order correction, which can be computed easily, can reproduce the results found using Green's functions with topography. We refer to this correction as the receiver elevation correction (REC). The REC is a method of accounting for the variations in distance between source and receiver caused by topography. This method was first explored by Williams and Wadge (1998, 2000) in a volcanic setting, and was found to be somewhat effective when considering a spherical deformation source with axial symmetry. The REC was implemented in a tectonic setting by some of these authors in Langer et al. (2019) and by Yang et al. (2019), but its efficacy in tectonic settings, which have a very different geometry from volcanic settings, has not been determined.

In this study, we aim to demonstrate that topography can have a significant impact on static slip estimates. To this end, we base our analysis on the study of the 2015 M_w 7.5 Gorkha, Nepal event and the 2010 M_w 8.8 Maule, Chile event. These earthquakes were chosen because the regions of Nepal and Chile represent two end-members of topographic structure (Figure 1). Nepal's topography consists of many mountains and valleys that are close to one another, while Chile is segmented into large topographic domains: the trench and abyssal plain below 4000m, the margin and coastal plain around sea-level and the Andes mountain range mostly above 1500m altitude. The two events also differ in their data coverage: while the Gorkha event occurred on a terrestrial fault that is well-constrained by numerous data covering the entire region of interest, the Maule earthquake is only constrained by data from the landward side of the fault.

For both events, we sample the possible slip parameters with a Bayesian approach, which allows us to thoroughly compare estimated slip models and to obtain detailed information on the posterior uncertainty of inferred parameters. We compare slip models estimated using Green's functions calculated with and without topography and with the receiver elevation correction. We first analyze these events within a synthetic framework to show that neglecting topography can lead to large biases in source estimates. We then use the real datasets to demonstrate how slip estimates are altered when neglecting topography for these particular events. Note that our aim here is to investigate the impact of topography on slip estimates for two particular events, not to produce the most realistic slip models of these events. We therefore make simple approximations for the other forward model parameters, such as fault geometry and elastic heterogeneity, to simplify our interpretations.

4
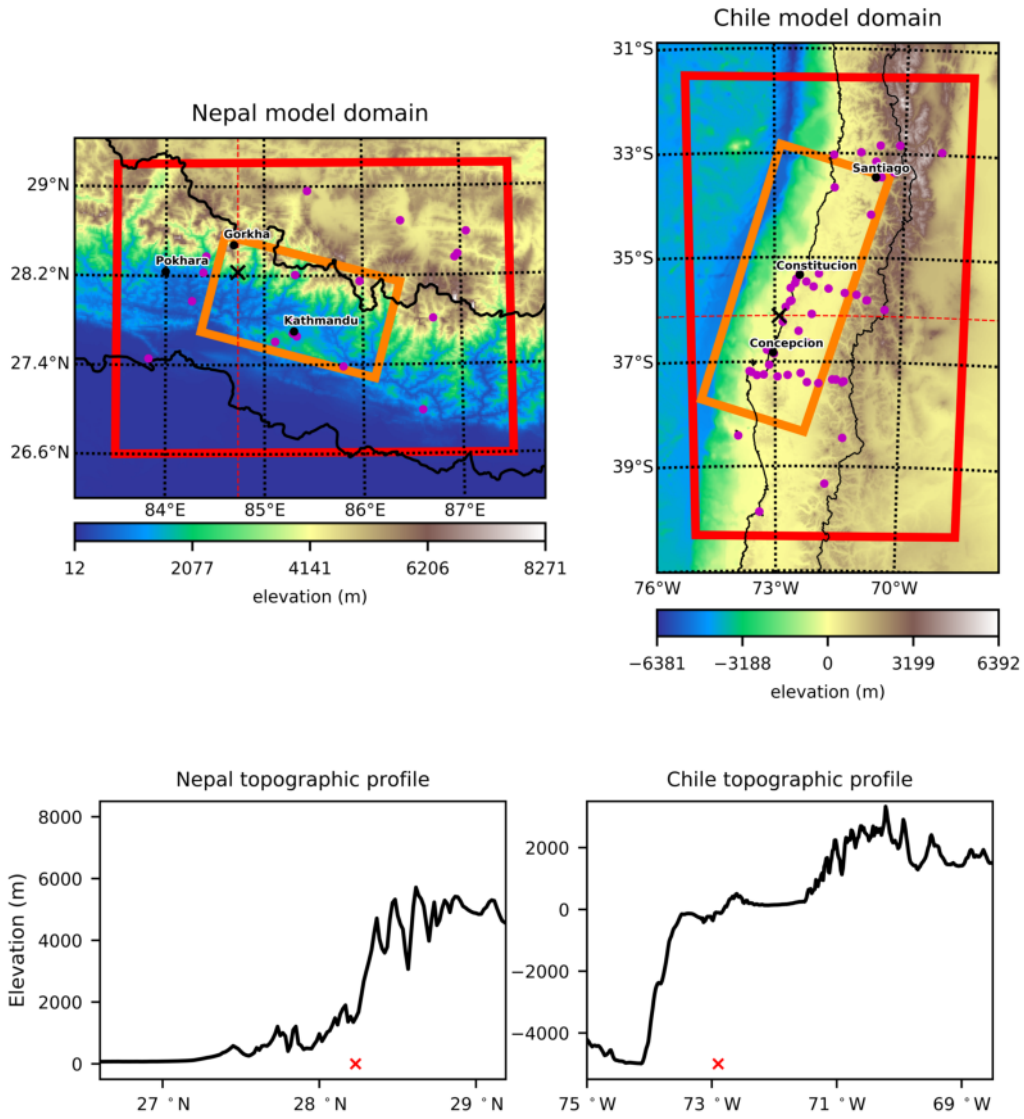
Figure 1: Topography of Nepal (left) and Chile (right). Red rectangles show the outlines of the meshes used to calculate Green's functions with topography for each of these regions. Orange rectangles show the outlines of the faults used in this study. Purple dots show the locations of the GPS stations. The black X symbols indicate the epicenters of the April 2015 Gorkha main shock and the February 2010 Maule main shock. Lower panels show topographic profiles for each region. The locations of the profiles are indicated by a red dashed line. Both profiles are near the epicenters of the two events, but the Nepal profile is north-south and the Chile profile is east-west so that the primary topographic features may be seen. The red X indicates the location of the epicenter along each profile.

2. Tools and methods

2.1. Generating 3D Green's functions

A coseismic Green's function G_{ij} is the displacement at a point i on the surface of a domain due to slip on a subfault j. Green's functions for a particular region may be calculated by dividing the fault into subfaults and calculating the displacement on the surface of the domain due to a unit quantity of slip on each subfault. In our study, we do not constrain rake in the inversion, so we must calculate Green's functions for one meter of slip along strike and one meter of slip along dip. Thus, we must perform two calculations of surface displacement for each subfault.

To calculate Green's functions, we use a software package called SPECFEM-X (Gharti et al., 2019). SPECFEM-X, which is based on the spectral-infinite-element method, uses the (un)coupled elastic-gravitational equations to solve quasi-static problems. Since our Green's functions require only calculations of coseismic deformation, we can neglect gravity. The governing equations then become

$$\boldsymbol{\nabla} \cdot \mathbf{T} + \mathbf{f} = \mathbf{0}. \tag{1}$$

Here, $\mathbf{T}$ is the incremental Lagrangian Cauchy stress and $\mathbf{f}$ represents external forces.

There are several ways to implement a fault in SPECFEM-X. In this study, we use the moment-density tensor fault implementation. Each subfault is subdivided into a grid of patches, and each patch has an associated moment-density tensor given by (Dahlen and Tromp, 1998)

$$\mathbf{m} = \Delta s \, \mathbf{C} : \hat{\mathbf{s}} \, \hat{\boldsymbol{\nu}}. \tag{2}$$

$\mathbf{C}$ is the elastic tensor at the location of the fault patch. $\mathbf{C}$ varies in a heterogeneous domain, but the models in this study are homogeneous, so for our purposes $\mathbf{C}$ is constant. $\hat{\boldsymbol{\nu}}$ is the normal vector and $\hat{\mathbf{s}}$ is the slip direction. In general, these vectors must be calculated for each patch, but this study uses uniform fault geometry, so $\hat{\boldsymbol{\nu}}$ and $\hat{\mathbf{s}}$ do not vary between patches. Δs is the slip magnitude. When calculating Green's functions, we set $\Delta s = 1$ m.

SPECFEM-X calculates deformation throughout the mesh volume. However, we only need Green's functions at the locations on the surface where we have observations. The displacements at each of these observation points due to each fault patch are combined into a single matrix of Green's functions, $\mathbf{G}$.

2.2. Receiver elevation correction

Despite the efficiency of SPECFEM-X, we cannot match the speed of Green's functions calculations performed with the elastic half-space analytical solution (Steketee, 1958; Mansinha and
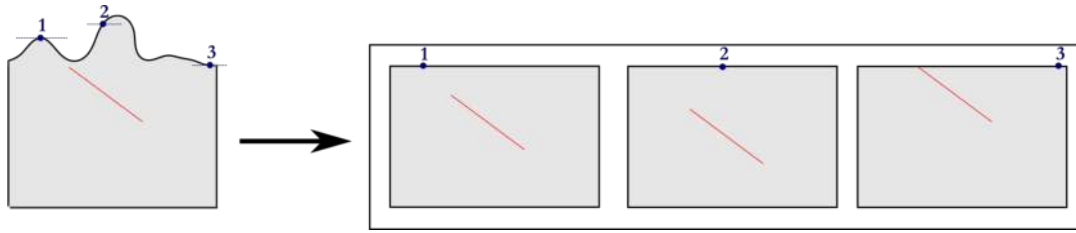
Figure 2: Green's functions with a receiver elevation correction are computed by calculating a separate homogeneous half-space solution for each point on the surface where Green's functions are needed. We would like to raise the flat surface to the elevation of the desired point (left). Since this is not possible, we lower the fault instead so that the distance between the fault and the surface is correct (right). For each homogeneous half-space setup in the right-hand panel, the Green's function is only calculated at the blue point on the surface.

Smylie, 1971). It would therefore be advantageous if there was a method of correcting the elastic half-space solution for topographic effects. There are two contributions to the topographic effect: the varying distance between the fault and the surface, and the elastic effects caused by the shape of the topographic surface (Williams and Wadge, 2000). The first of these effects can easily be accounted for by a zeroth-order correction which we refer to as the receiver elevation correction (REC), in which all calculations are done with the elastic half-space approximation but, for each receiver, with the fault raised or lowered to preserve its absolute distance to the receiver position if topography had been there. A diagram of this method is shown in Figure 2.

The REC is very easy to implement and can be calculated quickly, since it requires only a slight modification to the standard homogeneous elastic half-space calculation. However, in volcanic settings, it was found to not be a good approximation when topographic gradients are steep (Williams and Wadge, 2000); in this case, a more complicated semi-analytical solution or FEM must be used. We wish to determine whether the REC is a good approximation for topography in slip inversions of the Gorkha and Maule events. To this end, we calculate Green's functions for these events with the receiver elevation correction, and perform inversions to determine whether the REC can recover the result found with topographic Green's functions calculated with SPECFEM-X.

2.3. Bayesian sampling

Instead of trying to find a single solution to the inverse problem, we choose to sample the solution space and image a selection of its probable models. This sampling approach allows us to precisely compare various slip models and their posterior uncertainty. We do not incorporate any spatial smoothing that may bias or induce unwanted artifacts in inferred slip models (Du

7

^{146} et al., 1992; Beresnev, 2003; Aster et al., 2005; Causse et al., 2010; Gallovič et al., 2015; Gombert
^{147} et al., 2017). This choice will allow us to more precisely quantify the effects of topography. We
^{148} use the Bayesian sampling approach implemented in the AlTar package, which is a rewrite of the
^{149} code CATMIP (Minson et al., 2013). AlTar combines the Metropolis algorithm with a tempering
^{150} process to perform an iterative sampling of the solution space of source models. A large number of
^{151} samples are tested in parallel at each transitional step. Additionally, resampling is performed at
^{152} the end of each step to replace less probable models. The probability that a given sample will be
^{153} selected depends on its ability to fit the observations $\mathbf{d}_{\mathrm{obs}}$ within the uncertainties $\mathbf{C}_\chi = \mathbf{C}_{\mathrm{d}} + \mathbf{C}_{\mathrm{p}}$,
^{154} where $\mathbf{C}_{\mathrm{d}}$ represents the observational errors and $\mathbf{C}_{\mathrm{p}}$ the epistemic uncertainties introduced by
^{155} approximations of the forward model (e.g., Minson et al., 2013; Duputel et al., 2014; Ragon et al.,
^{156} 2018, 2019b).

^{157} The ability of each model parameter to solve the source problem is evaluated through repeated
^{158} updates of the Probability Density Functions (PDFs):

$$f(\mathbf{m}, \beta_i) \propto \ p(\mathbf{m}) \cdot \ \exp[-\beta_i \cdot \chi(\mathbf{m})], \tag{3}$$

^{159} where $\mathbf{m}$ is the current sample, $p(\mathbf{m})$ is the prior distribution on this sample, i corresponds to the
^{160} current iteration and β evolves dynamically from 0 to 1 to ensure an exhaustive exploration of the
^{161} solution space (Minson et al., 2013). $\chi(\mathbf{m})$ is the misfit function:

$$\chi(\mathbf{m}) = \frac{1}{2} [\mathbf{d}_{\mathrm{obs}} - \mathbf{G} \cdot \mathbf{m}]^T \cdot \mathbf{C}_\chi^{-1} \cdot [\mathbf{d}_{\mathrm{obs}} - \mathbf{G} \cdot \mathbf{m}]. \tag{4}$$

^{162} The final output from our Bayesian sampling procedure is a series of models sampled from
^{163} among the most plausible models of the full solution space. This set of samples provides information
^{164} on the possible parameter values and on their uncertainty. Average models (average value for every
^{165} parameter) are probabilistic values that do not correspond to a sampled model, but which can give a
^{166} good insight on the slip value of the most likely solutions. The posterior standard deviation of every
^{167} parameter informs on the amount of slip uncertainty associated with each subfault. More detailed
^{168} quantities, such as the marginal posterior distribution of a given parameter, reflect what has been
^{169} learned relative to our prior information. In particular, the shape and width of the posterior
^{170} marginal PDFs can be considered a proxy for the model resolution of the inferred parameter. To
^{171} visualize the results in the following sections, we plot average slip models and associated standard
^{172} deviations in map view, and the posterior marginal PDFs for a few representative subfaults. In
^{173} the following, we use the term spatial resolution when describing whether model parameters can
^{174} be independently resolved in theory (Menke, 2012, e.g.), and the term model resolution when
^{175} describing their associated uncertainty.

3. A continental thrust test case: The 2015 $M_w 7.8$ Gorkha, Nepal earthquake

On April 25, 2015, a magnitude $M_w 7.8$ earthquake occurred in central Nepal along the boundary between the Indian and Eurasian tectonic plates. This region is home to extreme topographic variations, and it is entirely terrestrial, so extensive data coverage from InSAR and GPS is available throughout the area of interest. These qualities make this earthquake an ideal event for a study on the impact of Green's functions with topography.

The 2015 Gorkha mainshock has been extensively studied with seismic and geodetic data (Wang and Fialko, 2015; Feng et al., 2015; Yagi and Okuwaki, 2015; Yi et al., 2017; Yue et al., 2017; Liu and Yao, 2018; Ingleby et al., 2020). Most studies recovered an inferred slip distribution consisting of an oval-shaped slip pattern with its center slightly northwest of Kathmandu and a small bulge to the northeast. The ruptured area was found to be approximately 150 km long, with a maximum slip of 6 m. Most of the previously published slip studies of this event used Green's functions calculated in a homogeneous half-space, with a few exceptions. Tung and Masterlark (2016) calculated Green's functions for the Gorkha event using a finite element model with heterogeneous crustal structure and realistic topography, and used those Green's functions to invert for a slip model using GPS and InSAR data. The resulting slip model was compared to one found using Green's functions with topography but homogeneous elastic structure. They found that the heterogeneous Green's functions yielded a slip model that fit their data better. However, they did not investigate the impact of topography. Similarly, Wang et al. (2017) compared slip models recovered using Green's functions calculated in a homogeneous half-space and in a heterogeneous, topographic domain. The two models had slightly different slip distributions and different slip amplitudes. However, their tests showed that the dominant effect was likely due to the heterogeneous elastic structure, which makes it difficult to determine the impact of topography in isolation. A study on the effects of topography was performed by Yang et al. (2019), which computed Green's functions with and without the receiver elevation correction. They found that the two resulting slip models differed in both slip amplitude and distribution. However, as we discussed in Section 2.2, the REC does not capture the full topographic effect and is not always a good approximation, especially when topographic gradients are large. Is this correction sufficient for the 2015 Gorkha earthquake? In this section, we seek to answer this question by assessing the full topographic effect on the static fault slip estimate.

Because of the good instrumentation of this event, combined with the fact that most of the slip occurred on a shallowly dipping part of the fault (see a more detailed explanation in Section 3.1.3), the coseismic deformation is unusually well constrained. This exceptional spatial resolution ex-

plains why the published slip models are almost all identical. With this in mind, we might ask whether the inclusion of topography is necessary to improve our slip models or the fit to our data. To answer this question, we invert for synthetic slip models to determine whether Green's functions with topography can truly improve inversion results.

The unusually high constraint on the slip distribution of the Gorkha event is not shared by most earthquakes, especially subduction events, which occur in areas with strong topographic gradients that are far from any terrestrial data. It is conceivable that the impact of topography may not be noticeable with lower slip resolution. We therefore also investigate the Gorkha event using only GPS data to find out whether our results can be generalized to a less well-constrained case.

3.1. Data and Forward Model

3.1.1. Data

Our geodetic data set contains static co-seismic offsets from 18 3-component continuous GPS stations and 4 SAR interferograms. The data points are scattered over our model domain. The GPS offsets were provided by Galetzka et al. (2015) and Yadav et al. (2017). One Sentinel-1 ascending frame was used, collected by the European Space Agency and processed by Grandin et al. (2015). Two ALOS-2 descending frames and one ALOS-2 ascending frame, collected by the Japan Aerospace Exploration Agency (JAXA), were processed by Lindsey et al. (2015). The InSAR data have been downsampled based on model resolution (Lohman and Simons, 2005), and the data errors have been calculated following Jolivet et al. (2012). A more detailed description of our data can be found in Section S1 of the Supplementary Material. Note that the surface displacements derived from the InSAR data contain between 8 and 9 days of post-seismic deformation, and that our GPS displacements are daily solutions, which might affect our modeling of the coseismic phase (e.g. Ragon et al., 2019a; Twardzik et al., 2019)

3.1.2. Crustal domain parameters

Our model domain extends from 83.5°E to 87.5°E and 26.6°N to 29.2°N. The mesh, shown in Figure S2, measures approximately $390 \times 280 \times 83$ km and has a mesh spacing of 3 km, for a total of 323830 elements. This mesh is used for all topographic Green's functions calculations, whether the full dataset or only GPS data are used. Each forward model calculation runs on 40 processors in approximately 5.2 minutes. The model domain has a Poisson's ratio of 0.25 and Young's modulus of 82.4 GPa. These are the material properties used for the homogeneous model of Nepal in Langer et al. (2019).

Our benchmarks, shown in Figure S3, showed that solutions produced by SPECFEM-X with

a flat mesh are nearly identical to those produced with homogeneous elastic half-space solutions (Okada, 1992) for coseismic deformation. Since homogeneous half-space calculations are much faster, we generated the Green's functions without topography using those analytical solutions. We choose to put the surface of the flat domain for the non-topographic Green's functions calculations at an elevation of 244 m, which corresponds to the elevation of the deepest point where the fault meets the surface in the topographic mesh.

3.1.3. Assumed MHT fault geometry

Many attempts have been made to determine the structure of the Main Himalayan Thrust (MHT) fault in Nepal. Some studies have found evidence that the MHT has a ramp-flat-ramp structure (Nábělek et al., 2009; Wang and Fialko, 2015; Elliott et al., 2016; Wang et al., 2017; Almeida et al., 2018b). Others have argued that instead of a lower ramp, the MHT has a duplex system of steeply dipping faults (Herman et al., 2010; Grandin et al., 2012; Mendoza et al., 2019). Others have found that a planar fault provides the best fit to the data for the 2015 Gorkha earthquake (Whipple et al., 2016; Wang and Fialko, 2018). Even if a ramp-flat-ramp structure does exist in the region of interest, it probably would not have a significant effect on our inversion because nearly all studies agree that the vast majority of slip took place on the flat section of the fault (Elliott et al., 2016; Wang and Fialko, 2018; Yang et al., 2019; Ingleby et al., 2020). Additionally, Ingleby et al. (2020) suggests that coseismic data do not require a shallow splay fault. Therefore, we have chosen to use a planar fault when generating Green's functions.

We assume a 180 km long and 100 km wide planar fault, with a strike of 285° and a dip of 7° northeast. Because the slip that occurred during this event did not reach the surface, we eliminated the upper section of the fault, so that the starting depth of the fault is at 3.9 km. For the inversions with the complete dataset, the fault is divided into a grid of 10 km × 10 km subfaults, so that there are 18 subfaults along strike and 10 subfaults along dip. When calculating Green's functions with topography using SPECFEM-X, we use 400 moment-density tensor patches for each subfault. Given the results of the tests presented in Gharti et al. (2019), this number of patches is more than enough to guarantee convergence.

When only GPS data are used, the spatial resolution is less. Therefore, we increase the size of each subfault to 15 km × 12.5 km. The fault has only 12 subfaults along strike and 8 subfaults along dip. When calculating Green's functions with topography using SPECFEM-X, we use 9216 moment-density tensor patches for each subfault. The other fault parameters are detailed in Table 3 of the Supplementary Material.

11

3.1.4. Other assumed prior information

We perform our static slip estimation as previously detailed in Section 2.3. We specify a zero-mean Gaussian prior $p(\mathbf{m}) = \mathcal{N}$(-1 m, 1 m) on the strike-slip component, since we assume that, on average, the slip direction is along dip. For the dip-slip component, we consider each possible value of displacement equally likely if it is positive and does not exceed 25 m of normal slip: $p(\mathbf{m}) = \mathcal{U}$(0 m, 25 m). We account for the data uncertainties as detailed in Section S1 of the Supplementary Material. We assume conservative uncertainty values of (-1°, 1°) around the prior value for the fault dip and (-1 km, 1 km) for the fault position.

3.2. Results

We first wish to investigate the impact of topography on slip models without contamination from potential uncertainties or bias that may result from our choices of crustal properties and fault structure, or from data errors. Therefore, we will start by analyzing the results of synthetic tests. This will allow us to determine whether Green's functions with topography can truly improve the inferred slip distribution. We will then use our inversion procedure to estimate slip models using real data from the Gorkha earthquake. In both cases, we will perform inversions using two datasets, one consisting of all data points from GPS and InSAR, and one with GPS stations only.

3.2.1. Synthetic tests

For the synthetic inversions with the full dataset, our target model, shown in Figure 3A, consists of five pure dip-slip patches of 6 m amplitude: four 20×20 km patches located at each corner of the fault, and a central patch 50 km long and 20 km wide. In the GPS-only case, shown in Figure 3E, the corner slip patches are 30 km long and 25 km wide, and the central slip patch is 60 km long and 25 km wide. Using a topographic domain and the fault geometry specified in Section 3.1.3, we compute the surface displacements induced by each of these target models at the data locations. We then solve for slip distributions with these synthetic data using Green's functions with and without topography. In our inversions, we assume the same fault geometry and crustal structure used when calculating the synthetic data. A first set of tests is done without noise added to the synthetic data, so that the inversion process is only perturbed by changes in the Green's functions. In another set of tests which are presented in Supplementary Material, we add white noise and spatially correlated noise (with a Gaussian covariance matrix of variance 1 and correlation length 10 km and 50 km) to the synthetic data, so that the noise amplitude reaches up to 10% of the maximum amplitude of the data. The assumed data error is the same as for the real dataset. We do not account for uncertainty in the fault geometry, since the geometry is perfectly known. The results of these tests are shown in Figures 3 and S5.
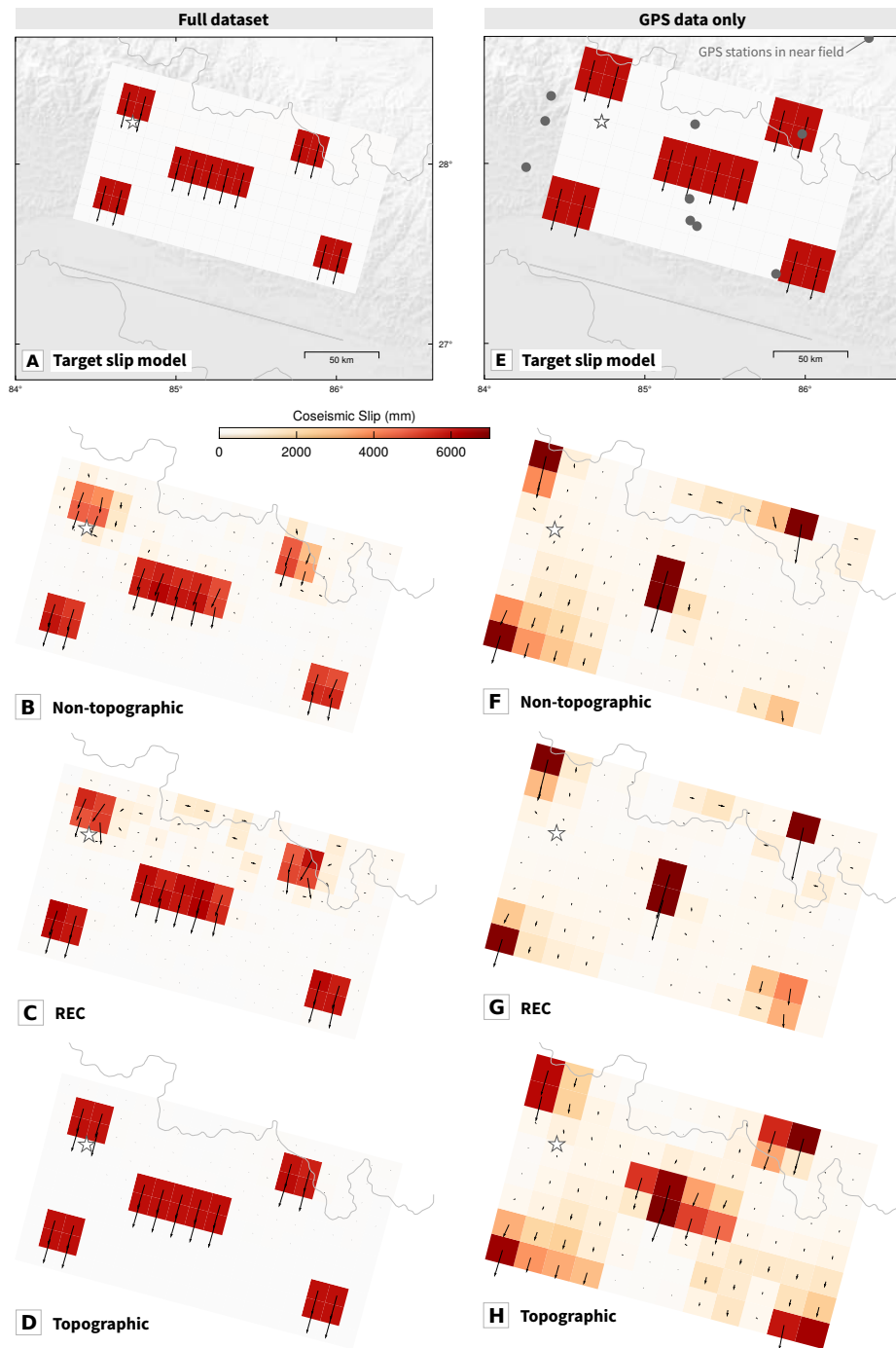
Figure 3: Comparison of slip models estimated from synthetic data for the Gorkha earthquake. (A) and (E): Target slip models used to calculate the full synthetic data set or synthetic GPS-only dataset, respectively. In (E), gray dots show the locations of the GPS stations. The remaining panels show average slip amplitude and rake inferred with non-topographic, REC and topographic Green's functions using the full synthetic data set (left columns) and synthetic GPS data only (right columns). Color scale is the same for all figures.

When the noise-free full synthetic data set is used, the slip model is perfectly recovered with topographic Green's functions (Figure 3D). When Green's functions without topography are used, only some slip patches are recovered (Figure 3B). The non-topographic Green's functions do especially poorly in the intermediate and deep sections of the fault, where topographic gradients are largest and where the data are less informative because the slip is farther from the location where the fault reaches the surface. If we use Green's functions with the receiver elevation correction (Figure 3C), the slip model is recovered better than with non-topographic Green's functions but not as well as when using Green's functions with topography. Results are even farther from the target model when using noisy data, with the exception of the topographic case, in which the target slip model is estimated fairly well (Figure S5).

When only GPS data are used, several slip patches can be recovered somewhat with topographic Green's functions (Figure 3H),and for most parameters, more than 30% of inferred values (and up to 60%) lie within 1.5 m of the non-zero target slip. None of the inversions can perfectly recover the target model, which is expected given that the data coverage is too poor to be fully compensated by increasing the size of the subfaults. However, the difference between the models estimated using Green's functions with and without topography is even more pronounced in this case. In particular, the non-topographic model fails to infer the eastern shallow slip patch, and concentrates the other slip patches into a fourth of their actual spatial distribution (Figures 3F, G), so that less than 10% of the inferred parameters lie within 1.5 m of the non-zero target slip. Interestingly, Green's functions with the REC produce a slip model very similar to the non-topographic result, and in fact seem to do an even poorer job in the shallow section of the fault. Inferred models are similar when using a noisy dataset (Figure S8).

Synthetic data are well fitted by the predictions of the inferred models, whether noise has been added or not (Figures S4, S6 and S7. However, only the models recovered with topographic Green's functions can explain the ∼10 cm uplift occurring where topographic gradients are greatest (around 29°N, Figure S4). The REC method, in contrast, does not significantly improve the fit to the synthetic data.

These synthetic tests show that the use of Green's functions with topography leads to a significant improvement in the recovered slip models. This is also true if realistic amounts of noise are added to the synthetic data, demonstrating that topographic effects are significant enough to affect an inversion with real data. Accounting for topography becomes even more necessary when the slip is not well-constrained due to poor spatial resolution since, in this case, use of non-topographic Green's functions leads to very poor estimates of the slip distribution. Green's functions with the receiver elevation correction were able to recover a better slip model than non-topographic Green's

14

₃₄₀ functions when the full dataset was used, but they performed more poorly in the GPS-only case.

₃₄₁ With this in mind, we will now analyze inferred slip distributions found with these different types

₃₄₂ of Green's functions using the real dataset from the Gorkha earthquake.

3.2.2. Inferred Slip Distributions with the Full Dataset

₃₄₄ Inferred slip distributions for the 2015 Gorkha earthquake found with the full dataset of GPS

₃₄₅ and InSAR data are shown in Figure 4. The main characteristics of the inferred slip distributions

₃₄₆ appear, at first glance, to be similar regardless of which type of Green's functions is used. The

₃₄₇ slip is concentrated in a well-resolved patch reaching 7 m in amplitude located near the center of

₃₄₈ our fault. Some deep slip can also be observed, particularly on the eastern side of the fault. This

₃₄₉ slip distribution is similar to previously published slip models for this event (e.g. Feng et al., 2015;

₃₅₀ Zuo et al., 2016). The main difference between the distribution of slip in the models is at depth:

₃₅₁ the topographic and REC models have more slip in the deeper part of the fault. The topographic

₃₅₂ and REC models also have slightly greater uncertainty in the deeper part of the fault.

₃₅₃ We can perform a more detailed analysis using Figure 4(D), which shows the marginal posterior

₃₅₄ Probability Density Functions (PDFs) for the subfaults selected in panels (A), (B) and (C). Overall,

₃₅₅ the posterior PDFs are narrow, especially in the shallowest part of the fault, because the slip is

₃₅₆ well resolved and restricted epistemic uncertainties are assumed. Topographic and REC PDFs

₃₅₇ have significant overlap, showing that their average slip values are very close. This is consistent

₃₅₈ with our findings in Section 3.2.1 that the REC can approach the topographic solution when the

₃₅₉ full dataset is used. In contrast, the PDFs which correspond to the inversion with non-topographic

₃₆₀ Green's functions do not even overlap with the topographic PDFs. This means that it is not only

₃₆₁ the average value that differs between these two inferred models; the full posterior distributions

₃₆₂ are different. Therefore, we cannot find a parameter value that satisfies both results; there is

₃₆₃ no latitude to reconcile non-topographic and topographic results. Our results might therefore

₃₆₄ imply that non-topographic models are inherently wrong (within the limitations of our study),

₃₆₅ because they are unable to capture the parameter values imaged with topography. However, it is

₃₆₆ important to note that in this study, we made simplified assumptions regarding fault geometry,

₃₆₇ crustal structure, and epistemic uncertainties. Additionally, for this particular event, the slip

₃₆₈ distribution is particularly well-constrained. If more realistic model characteristics and associated

₃₆₉ epistemic uncertainties were assumed, this would probably increase the posterior uncertainty and

₃₇₀ may enable reconciliation of non-topographic and topographic results.

₃₇₁ Figure 5 shows the fit to the observed data using predictions from the topographic model.

₃₇₂ These fits are quite good, but the observations are fitted well with any of our models. Additional

15
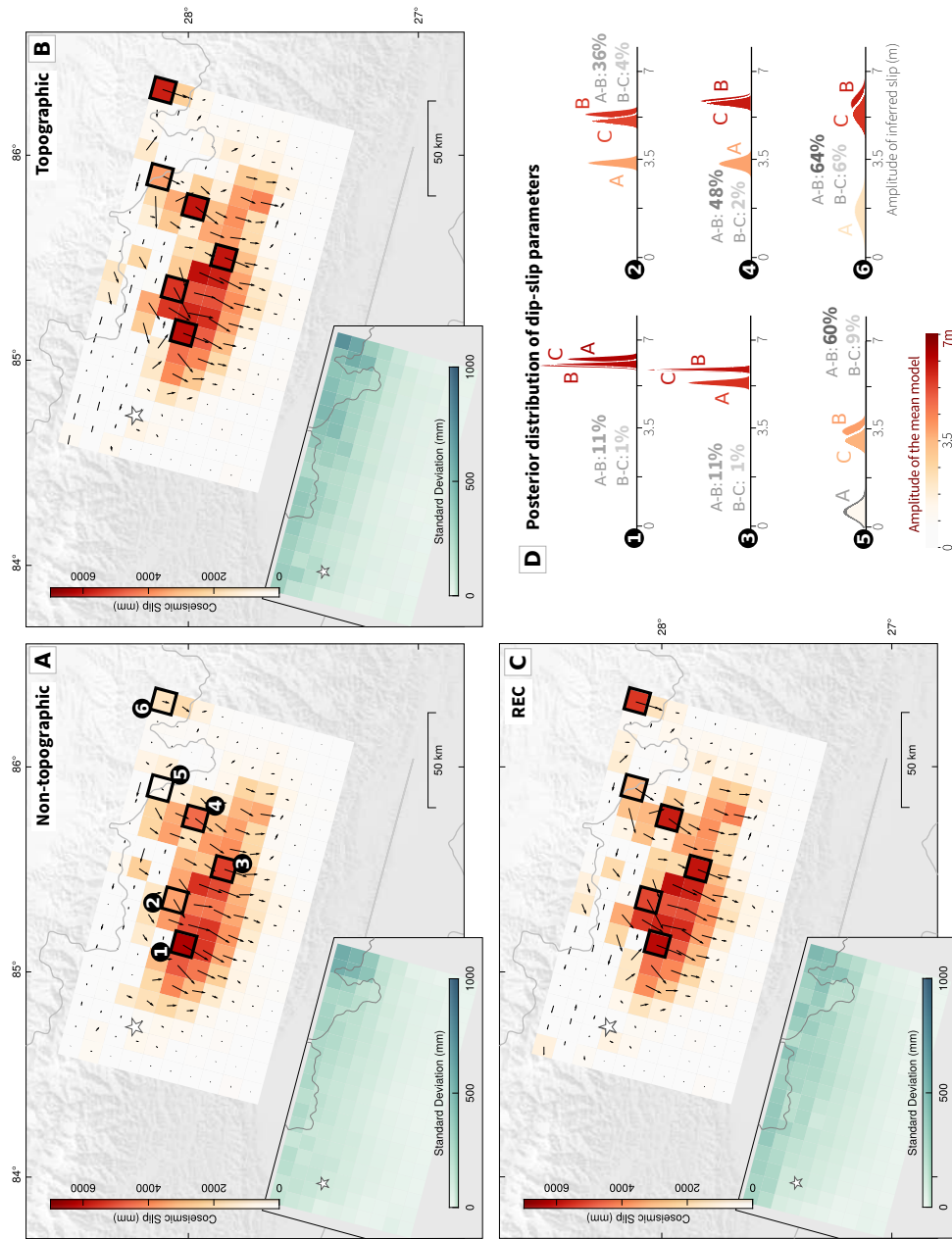
Figure 4: Comparison of finite-fault slip models of the 2015 Gorkha earthquake inferred with the complete dataset of GPS and InSAR data. Slip amplitudes are shown in red, and posterior standard deviations are shown in green. White star shows the location of the epicenter.(A) Map view of average slip amplitude and rake inferred with non-topographic Green's functions. (B) Average slip model inferred with topographic Green's functions. (C) Average slip model inferred with REC Green's functions. (D) Comparison between posterior marginal Probability Density Functions (PDFs) of dip-slip parameters for selected subfaults. PDF colors correspond to amplitude of the average model. Offsets between average models are shown as a percentage of slip amplitude. Plots of posterior PDFs are truncated between 0 and 7 m to simplify the visualization.

16
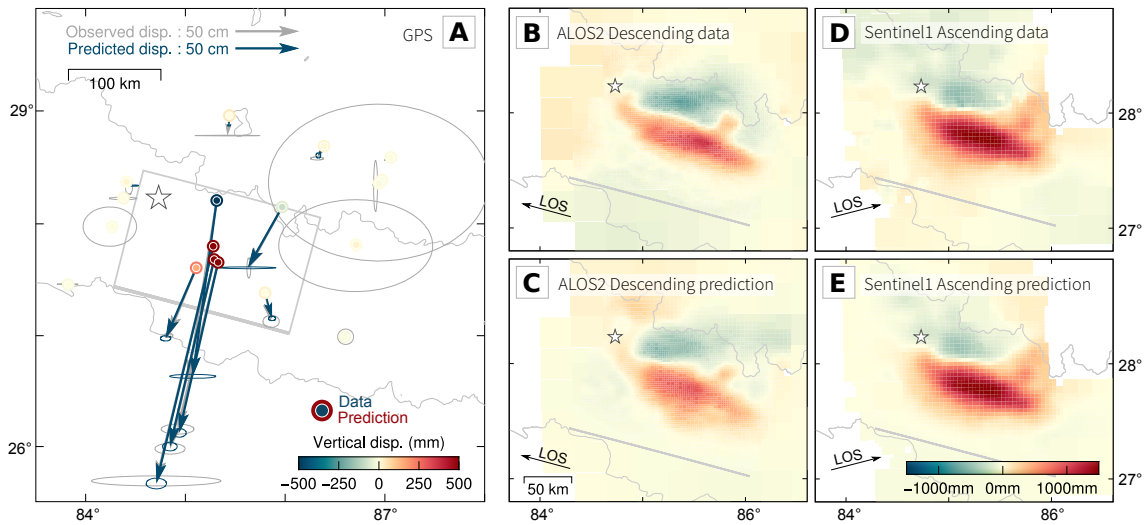
Figure 5: Fit to the observations for the topographic model of the 2015 Gorkha earthquake. (A) Observed and predicted static GPS offsets shown in map view. Observed horizontal surface displacements are in gray with 95% confidence ellipses, and predicted displacements are in blue with 95% confidence ellipses. Vertical displacements are color-coded with color-scale truncated at (-50 cm, 50 cm). The inner circle represents the data and the outer circle represents predicted displacements. (B) and (C), respectively: Observed and predicted surface displacement in the line of sight of the ALOS 2 descending interferogram. (D) and (E), respectively: Observed and predicted surface displacement in the line of sight of the Sentinel 1 ascending interferogram. The fault trace is represented as a gray line, and the epicenter as a white star.
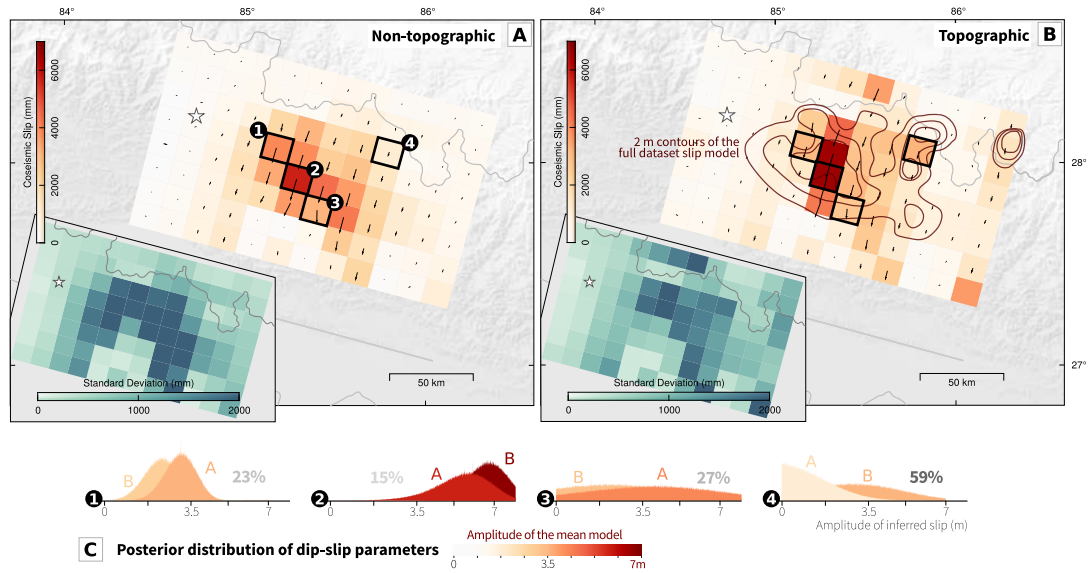
Figure 6: Comparison of finite-fault slip models of the 2015 Gorkha event estimated using the GPS-only dataset. Slip amplitudes are shown in red, and posterior standard deviations are shown in green. White star shows the location of the epicenter. (A) Average slip model inferred with non-topographic Green's functions. (B) Average slip model inferred with topographic Green's functions. (C) Comparison between posterior marginal Probability Density Functions (PDFs) of dip-slip parameters for selected subfaults. PDF colors correspond to amplitude of the average model. Offsets between average models are shown as a percentage of slip amplitude. Plots of posterior PDFs are truncated between 0 and 7 m to simplify the visualization.

figures can be found in the Supplementary Material: Figure S9 shows the fit to the GPS data, and Figures S10, S11 and S12 show the fits to the InSAR data for the non-topographic, topographic and REC models, respectively. Accounting for topography does not significantly improve the fit to the observed data.

3.2.3. Slip estimates with GPS data only

Figure 6 shows that when only GPS data are used, inversions using Green's functions with and without topography yield noticeably different slip distributions. The differences are especially pronounced in the center of the fault, where average slip is 1.5 m greater for the topographic model, and in the deepest part of the fault, which lies beneath the largest topographic variations. Given the results of our synthetic tests, we expect that the two high amplitude patches seen in the topographic model (Figure 6(B)) are probably of lesser amplitude. The selected posterior marginal Probability Density Functions (PDFs) shown in Figure 6(C) are very broad, and the PDFs from

18

the two inversions overlap significantly. As expected, the slip is thus less constrained than with the full dataset, so the posterior uncertainty is much greater, even with a coarser discretization of the fault plane. However, if the topography is accounted for, the location of large slip is similar whether the full dataset or GPS data only are used (Figure 6(B)).

3.2.4. Conclusion for the Gorkha earthquake

Our synthetic tests for the Gorkha event suggest that the impact of topography can depend on spatial resolution of slip. When the slip is well constrained by geodetic data, neglecting topography will lead to incorrect slip estimates where topographic gradients are large, but with limited biases due to the great data constraints. Only incorporating topography will yield correct results. Where topographic variations are mild, estimates are correct whether topography is accounted for or not. On the other hand, when the slip is poorly constrained (GPS only), neglecting topography has a large impact on the inferred slip distribution. In this case, the REC approximation is not sufficient.

In our inversions with real data, topography mostly impacts the amplitude of the main slip patch and the mid-crustal part of the fault, where larger slip values are imaged. The topographic effect could thus explain why there is not yet a consensus on the mid-crustal geometry of the Main Himalayan Thrust (see references in Section 3.1.3).

Altogether, our results suggest that accounting for topography is necessary when topographic variations are significant, even if good data coverage can limit the biases induced by neglecting topography.

The Gorkha earthquake is an unusual type of dip-slip event with a very shallow dip angle and good data coverage directly above the fault plane. Our preferred slip model thus does not vary much when topography is accounted for, because most of the slip is located where topographic gradients are low and data are informative.

This type of good data coverage generally does not exist for subduction events, where the greatest amount of slip often occurs several tens of kilometers away from the coast, while all observations are on land, and at very different elevations from the trench (up to 6 km in some cases). In the following section, we investigate the 2010 $M_w 8.8$ Maule, Chile, earthquake to determine whether these results hold for a subduction setting.

4. A subduction megathrust test case: the $M_w 8.8$ 2010 Maule, Chile, earthquake

The second earthquake that we investigate is the $M_w 8.8$ 2010 Maule, Chile earthquake. This event occurred at the interface between the Nazca and South-American plates, within a region previously recognized as a seismic gap (e.g., Comte et al., 1986; Nishenko, 1991; Ruegg et al.,

19

2009; Madariaga et al., 2010). The slip distribution of this event was studied using geodetic, seismic and/or tsunami data (e.g., Delouis et al., 2010; Vigny et al., 2011; Lay, 2011; Lin et al., 2013; Yue et al., 2014; Yoshimoto et al., 2016).

Our choice of the Maule event was guided by the fact that it is a major and well studied event. It is also located on a subduction zone with a intermediate width (distance from the coast to the trench) of about 100 km. In the most favorable cases, like the Costa Rica and Sumatra subductions, this distance can be reduced to 20 to 30 km, while in cases like Tohoku/North Japan, it is closer to 200 km.

The Maule region, and subductions zones in general, differ from the Gorkha case in three critical ways. First, there are no near-field observations to constrain the shallow slip because it usually occurs far from the coast. Imaging slip on the fault requires sampling the gradient of the surface deformation, but in cases like Maule, the distance between parts of the fault and some observations can be greater than 200 km. The second major difference is that all data are on one side of the fault (landward) and some distance away from it, thus only covering a fraction of the surface deformation field. Any epistemic error will thus appear as a systematic bias in the Green's functions and is more likely to distort the model space. The third major difference is that observations are spread over two major topography domains, the coastal plain and the Andes mountain range (Figure 1). For both Gorkha and Maule, there are major short-wavelength topographic variations (40° slopes over distances of a few km), but a good data coverage across these variations might limit their impact on estimated slip, even if topography is not accounted for in the Green's functions.

The 2010 Maule earthquake has been intensively studied, and its rupture has been consistently modeled as bilateral, extending over 500 km along strike. Most of the inferred rupture models show two main slip patches located around longitudes of 35°N and 37°N, with the northern-most patch having higher slip amplitudes. Since the available geodetic data are located onshore, on one side of the rupture and far from the trench, derived rupture characteristics are poorly resolved near the trench. This lack of model resolution may explain why most geodetic studies find that the rupture did not reach the shallowest parts of the fault (e.g., Tong et al., 2010; Pollitz et al., 2011; Vigny et al., 2011; Lin et al., 2013) when direct (Maksymowicz et al., 2017) and indirect (Sladen and Trevisan, 2018) observations indicate the opposite. One exception to these geodetic models is the one of Moreno et al. (2012), which imaged a northern slip patch reaching the trench with 5 m amplitude. Conversely, most studies using seismic data do image moderate slip amplitudes (6-10 m) at the trench (e.g., Delouis et al., 2010; Lay et al., 2010; Koper et al., 2012; Ruiz et al., 2012). This is also supported by deep ocean tsunami data, which are located offshore and on the other

20

side of the rupture, and can provide better resolution at the trench (Yue et al., 2014; Yoshimoto et al., 2016). Earlier coseismic slip models relying on these tsunami data were probably biased by the fact that they did not consider long wavelength dispersion (e.g., Tsai et al., 2013; Watada et al., 2014; Yue et al., 2014).

Most of the published slip models for the Maule event do not account for the effects of topography and bathymetry. Moreno et al. (2012) did account for these effects using a spherical finite element model, and they imaged slip near the trench using geodetic data only. Would this mean that Green's functions with topography can increase the accuracy of slip models near the trench? In the following section, we will investigate the effects of topography and bathymetry on inferred slip distributions of the 2010 Maule earthquake.

4.1. Data and Forward Model

4.1.1. Data

Although there are GPS and InSAR data available for the Maule earthquake, we choose to rely on GPS data only for the sake of simplicity and because of the great coverage already provided. The results of Moreno et al. (2012) suggest that although adding InSAR data to the inversion procedure improves the calculated spatial resolution at the trench by 15-20%, it does not lead to a change in the inferred slip model. Our data consists of 53 static daily offsets processed by Vigny et al. (2011), and continuous GPS and survey sites processed by Lin et al. (2013).

4.1.2. Crustal domain parameters

Our model domain extends from -75.0°E to -68.5°E and -40.3°N to -31.5°N. The mesh measures approximately $553 \times 958 \times 136$ km and has a mesh spacing of 6 km, for a total of 318400 elements. A single forward calculation with this mesh runs on 40 processors in approximately 7.5 minutes. An image of the mesh is shown in Figure S13. The model domain has a Poisson's ratio of 0.25 and Young's modulus of 100.0 GPa. These are the material properties used for the homogeneous model of Chile in Langer et al. (2019). This mesh was only used to generate the Green's functions with topography. For the Green's functions without topography, we used the homogeneous half-space solution at 0 km elevation.

4.1.3. Geometry of the assumed fault

The portion of the slab that ruptured during the Maule earthquake can be approximated as a planar surface, with the exception of a change in strike at around 34°S (Hayes et al., 2018). We chose to assume a planar fault geometry. Given that our models have almost no inferred slip in the northernmost part of the fault (see Figure S19 of the Supplementary Material), this approximation

might not affect our slip estimates. Our fault is 570 km long and 240 km wide, with a strike of 198° and a dip of 18°. Since the slip is very poorly constrained near the trench, we experimented with two different fault parameterizations. The first one has homogeneous subfaults measuring 43.8 km along strike and 24 km along dip, and in the other parameterization, the two shallowest subfault rows have been merged into 8 bigger subfaults measuring 81.4 × 48 km. For all subfaults, we use 16900 moment-density tensor patches per subfault when calculating topographic Green's functions with SPECFEM-X. The first parameterization has extremely poor model resolution, so in the main text, we only present the results inferred with the second parameterization. The fault geometry parameters are detailed in Table 5 of the Supplementary Material.

4.1.4. Other assumed prior information

We perform our static slip estimation as previously detailed in Section 2.3. We specify a zero-mean Gaussian prior $p(\mathbf{m}) = \mathcal{N}(\text{-2 m, 2 m})$ on the strike-slip component, since we assume that, on average, the slip direction is along dip. For the dip-slip component, we consider each possible value of displacement equally likely if it positive and does not exceed 60 m of normal slip: $p(\mathbf{m}) = \mathcal{U}(0 \text{ m},$ 60 m). We account for the data uncertainty and for the uncertainty due to our a priori assumed fault geometry (Ragon et al., 2018, 2019b). We assume conservative uncertainty values of (-2°, 2°) around the prior value for the fault dip and (0 km, 2 km) for the fault position.

4.2. Results

We will first present the results of synthetic tests, which enable us to analyze the impact of topography on slip estimates without contamination from assumptions made when calculating Green's functions and from data errors. Then we will examine the results of our slip estimates for the Maule earthquake to determine whether Green's functions with topography can impact slip distribution, particularly near the trench.

4.2.1. Synthetic Tests

Our target model for the synthetic tests, shown in Figure 7A, consists of five $\sim 80 \times 48$ km pure dip-slip patches of 20 m amplitude. These slip patches are located near the trench and at intermediate depth. Using the fault geometry specified in Section 4.1.3, we compute surface displacements due to our target model at the data locations in a topographic domain. We then solve for the slip distribution using these synthetic data and the same fault geometry and crustal structure that were used to generate the data. The resulting slip models found using Green's functions without topography, with the receiver elevation correction, and with topography are shown in Figures 7B,C, and D, respectively. One set of tests is performed with noise-free data and
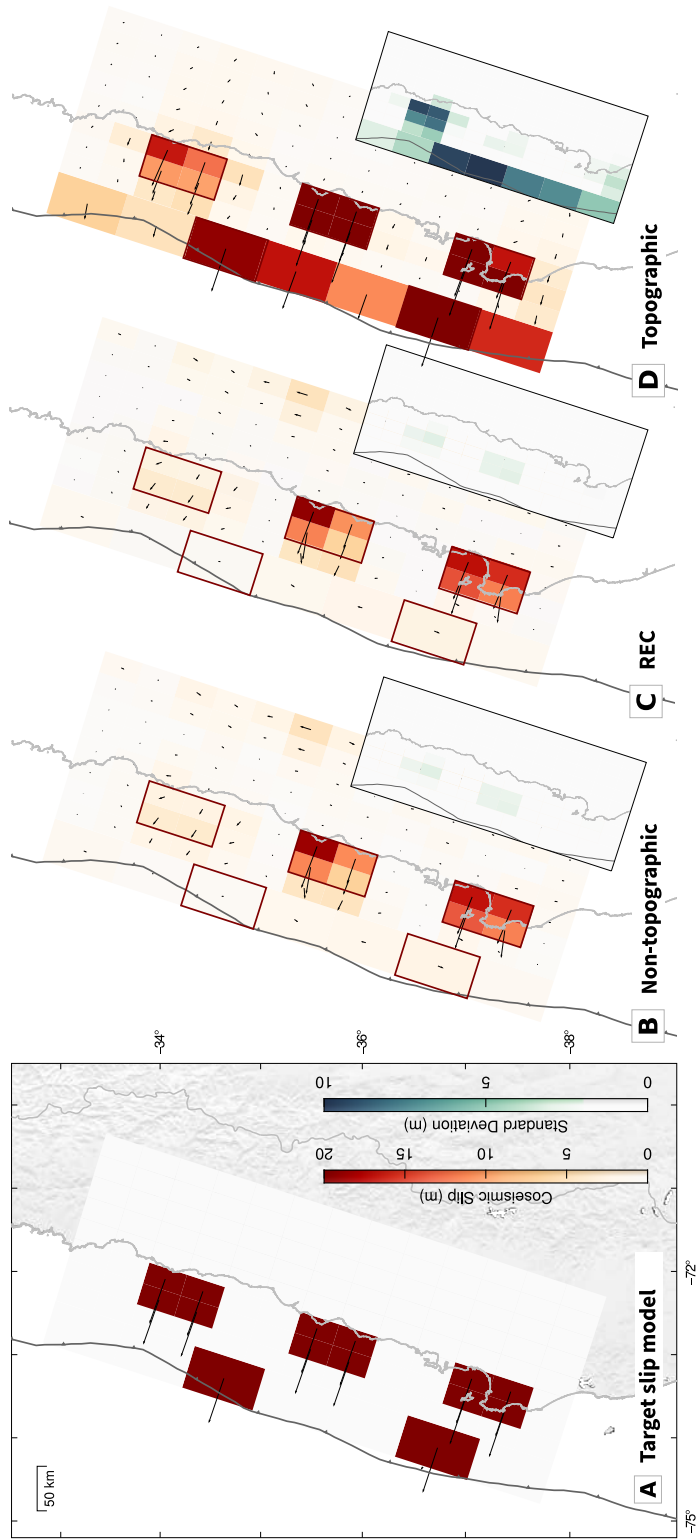
Figure 7: Comparison of slip models estimated from synthetic data for the Maule earthquake. (A) Target slip model used to calculate the synthetic data. (B), (C) and (D), average slip amplitude (red color scale) and rake estimated with non-topographic, REC and topographic Green's functions, respectively. Posterior standard deviations are shown in green at the bottom right of each slip model.

23

presented in the main text. For another set of tests, presented in the Supplementary Material, we add white noise and spatially correlated noise (with a Gaussian covariance matrix of variance 1 and correlation length 10 km and 50 km) to the synthetic data, so that the noise amplitude can reach up to 10% of the maximum amplitude of the data. The assumed data error is the same as for the real dataset. We do not account for error due to uncertainty in the fault geometry, since it is perfectly known.

Inversions with non-topographic and REC Green's functions fail to capture the target slip model whether noise is added to the synthetic data or not (Figures 7B,C and S14). Only two intermediate depth slip patches are even slightly recovered, with 15 to 70% of inferred values within 5 m of the target, likely because those patches are located closer to the shore and are therefore better resolved. The accuracy is very poor near the trench: estimated slip amplitude is less than 3 m, and the standard deviations are low, so that 100% of inferred values fall out 5 m of the target. Interestingly, the REC model is almost identical to the non-topographic model. This may be due to the poor spatial resolution at the trench, since a similar result was found with the GPS-only synthetic test of the Gorkha event (Figure 3H). An additional factor may be the steepness of the trench; Williams and Wadge (2000) showed that the REC does not work when topographic gradients are large. This result is also consistent with the findings of Langer et al. (2019) that lowering the surface of a flat mesh to the elevation of the seafloor does not allow one to capture the forward modelling result found with a topographic mesh for the Maule earthquake.

In contrast, the use of topographic Green's functions improves the recovery of the target model (Figures 7D and S14). The two intermediate depth patches that were somewhat recovered by the non-topographic and REC models are well-estimated in the topographic model, with almost 100% of inferred values within 5 m of the target, and the northernmost intermediate depth slip patch is retrieved too, although with a larger posterior uncertainty, so that more than 15% of inferred parameters are less than 5 m away from the target value. Near the trench, we infer large slip amplitudes with large standard deviations reaching up to 75% of the slip amplitude, from 30% to 65% of inferred parameters being within 5 m of the non-zero target. The two patches with the highest slip amplitudes and relatively low posterior uncertainties match the target slip patches. However, we also infer large amplitudes for neighboring subfaults, possibly because the information carried by the topographic Green's functions is too weak to differentiate the target patches from the neighboring subfaults. But this implies that the information brought by the topography allows us to infer that some slip was shallow. Note that adding realistic noise to the data leads to poorer estimates, which nonetheless remain closer to the target model than when no topography is accounted for, especially when considering the posterior uncertainty of inferred parameters

24

⁵⁴⁹ (Figure S14). To get rid of the possible correlation between slip patches, we also perform some
⁵⁵⁰ tests with independent patches. With only two near-trench target slip patches (Figure S16), we find
⁵⁵¹ that only introducing topography allows us to recover the target model reasonably well, although
⁵⁵² its amplitude is overestimated where the spatial resolution is correct, and underestimated to the
⁵⁵³ north. Similarly, with only two mid-crustal target slip patches (Figure S17), topographic Green's
⁵⁵⁴ functions do a better job at recovering the target model, but in this case, the non-topographic slip
⁵⁵⁵ model is close to the target model too. This is probably because the topographic gradients are
⁵⁵⁶ more mild in this mid-crustal location.

⁵⁵⁷ The synthetic data are explained well by the predictions of all of our models, whether topog-
⁵⁵⁸ raphy is accounted for or not, and whether noise is added or not (Figures S18 and S15). However,
⁵⁵⁹ only the topographic slip model can recover the synthetic secondary zone of uplift, corresponding
⁵⁶⁰ to ∼20 cm of upward surface displacement located east of 72°W.

⁵⁶¹ The results of these synthetic tests are similar to our findings for the Gorkha event: Green's
⁵⁶² functions without topography are unable to recover target slip where topographic variations are
⁵⁶³ large, and in particular where spatial resolution is low (here, the northern part and at the trench),
⁵⁶⁴ even when the receiver elevation correction is used. When Green's functions with topography are
⁵⁶⁵ used, the accuracy of the slip model is improved, regardless of the level of data coverage.

4.2.2. Slip Estimates

⁵⁶⁷ Using the real data from the 2010 Maule event, we now invert for slip models using non-
⁵⁶⁸ topographic, REC and topographic Green's functions. The inferred slip models, shown in Figure 8,
⁵⁶⁹ are all characterized by two main high-amplitude slip patches located at intermediate depth, around
⁵⁷⁰ 35° S and 37° S. This slip distribution is similar to the ones found by previous studies discussed
⁵⁷¹ in Section 4. The non-topographic and REC models (Figures 8A,B) are nearly identical, with
⁵⁷² large slip amplitudes of up to 20 m near the trench in the southern half of the fault, and some
⁵⁷³ slip estimated on the deepest row. The slip appears well constrained in the southern half of the
⁵⁷⁴ fault, with reasonably small standard deviations (Figure 8D, subfaults (1) and (3)). Posterior
⁵⁷⁵ uncertainty is higher for the northern half of the fault, with larger or Dirichlet-shaped posterior
⁵⁷⁶ PDFs (Figure 8D, subfaults (2), (5) and (6)).

⁵⁷⁷ The topographic slip model (Figure 8C) is very different from the two other results. The two
⁵⁷⁸ intermediate-depth high slip patches still have large amplitudes (up to 20 m), but there are also
⁵⁷⁹ intermediate-depth subfaults with moderate slip amplitudes in between those two patches. The
⁵⁸⁰ most striking difference is that only the northern slip patch reaches the trench, with up to 17 m
⁵⁸¹ of slip, and very small slip amplitudes are inferred near the trench in the southern half of the
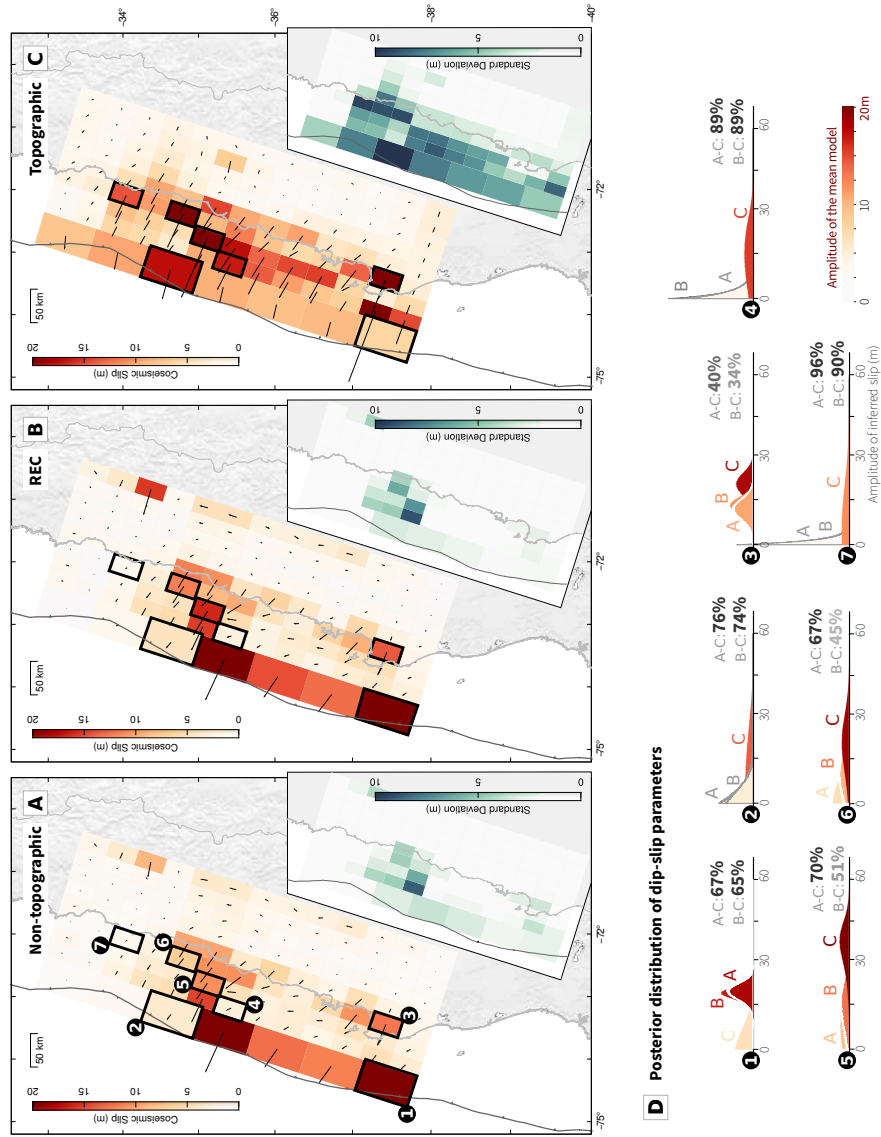
Figure 8: Comparison of finite-fault slip models of the 2010 Maule earthquake. Slip amplitudes are shown in red and posterior standard deviations for each slip model are shown in green. (A) Average slip amplitude and rake inferred with non-topographic Green's functions. (B) Average slip model inferred with REC Green's functions. (C) Average slip model inferred with topographic Green's functions. (D) Comparison between posterior marginal Probability Density Functions (PDFs) of dip-slip parameters for selected sub-faults. PDF colors correspond to amplitude of the average model. Offsets between average models are shown as a percentage of slip amplitude. Plots of the posterior PDFs are truncated between 0 and 60 m to simplify the visualization.

26

fault. Overall, posterior uncertainties (Figure 8D) are larger, and can often be greater than 50% of the slip amplitude. Given the results of the synthetic tests presented in the previous section, the topographic slip model is the only one able to provide meaningful results, even if associated with greater uncertainties. We note that this model is also coherent with the tsunami data (e.g., Yue et al., 2014; Yoshimoto et al., 2016), outer-rise aftershock distribution (Sladen and Trevisan, 2018) and a differential bathymetry study (Maksymowicz et al., 2017). Again, from the synthetic tests, we can suggest the medium slip amplitudes (5-10 m) along the trench are probably artefacts (also because the mean of the Dirichlet shape of the PDFs does not reflect the posterior mean), but the high amplitude patch ($\sim$17 m) imaged above the northern patch is likely realistic.

The slip model with the receiver elevation correction shows behavior that is consistent with the results of our synthetic tests. Average slip values for the REC model are approximately halfway in between average non-topographic and topographic slip values for intermediate depth subfaults (Figure 8D, subfaults (3) to (6)), but is very close to the non-topographic slip values for the near-trench subfaults (Figure 8D, subfaults (1) and (2)). This suggests that the REC only improves our estimates where spatial resolution is large enough, and is not effective at the trench where resolution is too low.

As discussed in Section 4.1.3, we performed similar slip inversions using a fault parameterized with homogeneous subfaults. This fault parametrization also yields very different results with topographic and non-topographic Green's functions, particularly near the trench where average slip reaches 20 m of amplitude for the non-topographic and REC models, but is close to 0 m in the topographic model (Figure S19 of the Supplementary Material). However, the near-trench posterior PDFs for the non-topographic and REC models are close to the uniform distribution (Figure S19D, subfaults (2) and (3) in particular), implying that the model resolution at the trench is so poor that the results are not meaningful. However, the resolution is better in the topographic model.

The fit of our model predictions to the data are shown in Figures 9 (for topographic and non-topographic Green's functions) and S20 (for REC Green's functions). Vertical and horizontal displacements appear to be well explained by both non-topographic and topographic models. There are two West-East rows of stations that can be used to investigate the fit in more detail. The predicted horizontal displacements are similar for both the topographic and non-topographic models, and both provide a good fit to the observations within the data errors and the posterior uncertainties of the predictions (Figure 9). However, the non-topographic model has difficulty explaining the complex shape and amplitude of uplift near the shoreline for both profiles: data points fall outside the prediction zone, which is shown as a gray area around the profiles. In con-

27
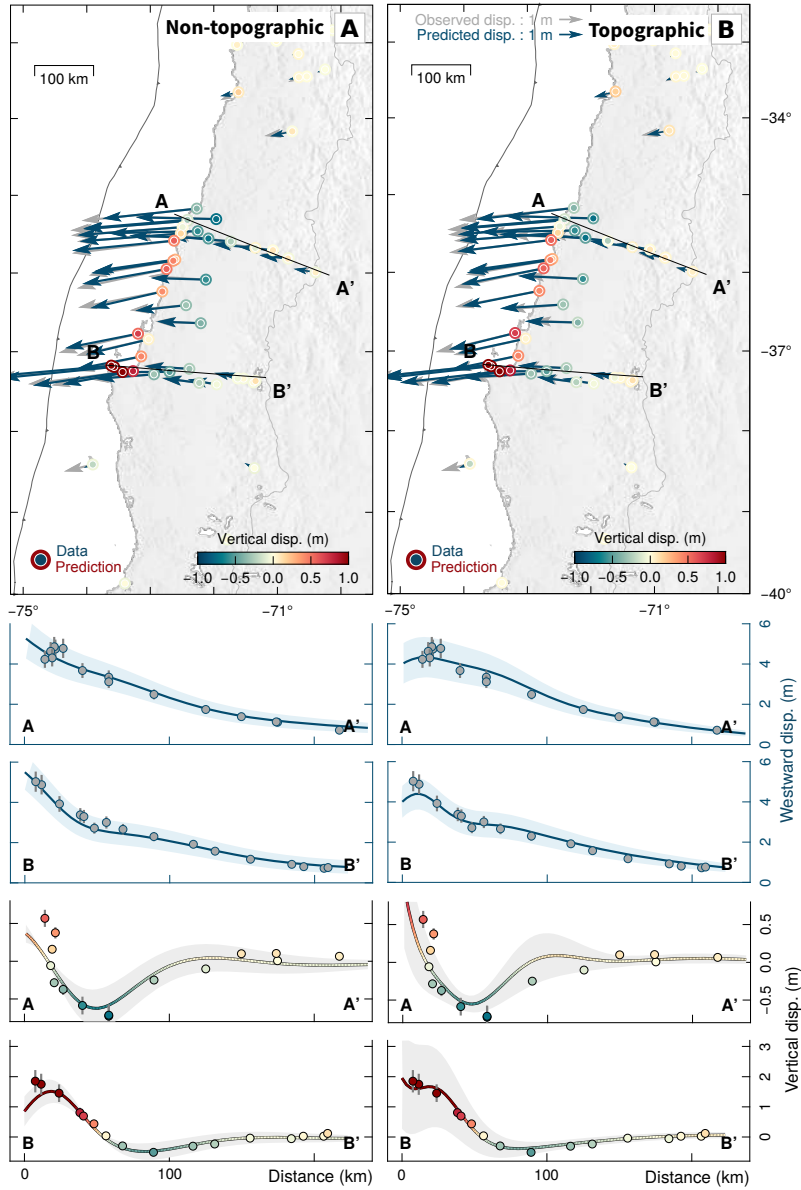
Figure 9: Comparison between static GPS offsets and predicted surface displacements for slip models of the Maule earthquake. Top panels show horizontal and vertical displacements in map view, along with predictions from non-topographic (A) and topographic (B) models. Inner circles show the data and outer circles show predictions. Observed horizontal surface displacements are in gray with 95% confidence ellipses, and predicted displacements are in blue with 95% confidence ellipses. Vertical displacements are color-coded with color-scale truncated at (-1 m, 1 m). Lower panels: Profiles A-A' at 35.5°S and B-B' at 37.5°S. For each profile, horizontal displacements are shown with gray dots and error bars for the data and a blue line with light blue area for predictions and associated posterior uncertainties. Vertical displacements are represented with the same color scale as in the map view, with dots and error bars for the data and a line with light gray area for predictions and uncertainties.

trast, the topographic model provides a better fit to the observed vertical surface displacement, especially near the coast. Note the large difference between the prediction uncertainties for the vertical displacements in the topographic and non-topographic profiles. This is because posterior slip uncertainty is greater in the topographic model, especially at shallow and intermediate depths.

4.2.3. Conclusion for the Maule earthquake

Our investigation of the Maule event indicates that the use of topographic Green's functions significantly affects slip estimates. Our synthetic tests demonstrate that topography is required to accurately infer slip distribution where gradients are steep, particularly if spatial resolution is low, e.g. at the trench and in the northernmost region of the fault. In our inversions with real data, only the topographic Green's functions allow us to explain some features of the vertical displacement data. Therefore, both the synthetic tests and the better fit to the observations seem to indicate that the average topographic slip model represents a better estimate of coseismic slip of the Maule event, even if the associated posterior uncertainties are larger. Our results also demonstrate that the receiver elevation correction is not a sufficient proxy for topographic Green's functions, especially for areas where slip is poorly constrained and topographic gradients are large, such as near the trench.

5. Discussion and Conclusions

Topographic variations are rarely accounted for in finite fault slip inversions, even when earthquakes take place in regions with extreme topography. Previous research (e.g., Hsu et al., 2011; Langer et al., 2019) showed that topography can have a significant effect on estimated surface displacements. In this study, we extended that work by assessing the effect of topography on static earthquake slip inversions.

With SPECFEM-X, a quasi-static spectral element software package, we are able to efficiently compute Green's functions in a topographic domain. We used SPECFEM-X to investigate the impact of topography on two earthquakes that represent two different types of topography and geodetic data coverage: the $M_w7.8$ 2015 Gorkha and $M_w8.8$ 2010 Maule earthquakes. The study of the Gorkha event is motivated by its exceptionally strong observational constraints and the fact that the highest amplitude slip occurs away from the greatest topographic gradients. On the other hand, the Maule earthquake is characterized by a large amount of slip occurring away from the data (especially near the trench), where topographic gradients are very high. The slip of the Maule event is also more poorly constrained because data are only available on the landward side of the fault.

For these two events, we compared slip models estimated with a Bayesian sampling approach using Green's functions calculated with topography, without topography, and with a zeroth-order topographic correction. We first investigated these events in a synthetic framework, and then we used the real datasets.

5.1. Impact of topography on slip models

Our synthetic tests for these earthquakes demonstrate that neglecting topography where gradients are large leads to incorrect slip estimates. In most cases, the target slip model is not even among the possible models recovered in an inversion with non-topographic Green's functions. However, if the observational constraints are very good (which is only true in rare cases), the biases introduced by the lack of topography might be limited. For instance, the locations of mid-crustal slip patches on the Main Himalayan Thrust are well-resolved, though the amplitudes are locally off by up to 80%. In contrast, where data coverage is less, artifacts caused by the absence of topography are more significant. For instance, when neglecting topography, we are unable to recover large slip amplitudes (20 m) at the trench for the Maule subduction event.

For both earthquakes, the use of Green's functions with topography produced different slip distributions. For the Gorkha event, this difference was relatively minor when the full dataset was used, probably because most of the slip is located where topographic gradients are mild. The impact of topography is more pronounced in slip models of the Maule earthquake. Accounting for topography leads to slip amplitudes and distributions that differ for every region of the fault, and in particular near the trench, where data are uninformative and topographic gradients are large. Interestingly, we also note that introducing topographic Green's functions leads to larger posterior uncertainties where the observational constraints are low. This is probably because assuming a more realistic forward model broadens the range of possible solutions, which can become even larger if the slip is poorly constrained. In contrast, assuming an incorrect forward model (without topography) leads to an incorrect sampling of the solution space and overfitting of the observations.

For both events, topographic Green's functions allow us to improve the consistency of the predictions with the observations. In particular, we find that topographic results are the only ones able to explain complexities in the surface uplift for the Maule event.

Given the results of our synthetic tests and the improved fit to observations, we may infer that slip models estimated with topographic Green's functions probably represent more accurate estimates of coseismic deformation than slip models estimated without topography. We note, however, that the forward model assumptions that we made, such as planar fault geometry and homogeneous crustal structure, and the other prior choices that were made in this study, such as

681 our parameterization of the forward problem, may also affect our estimates, so further study is
682 required to determine the effect of these factors.

683 *5.2. Effectiveness of the receiver elevation correction*

684 The receiver elevation correction (REC) accounts for variations in distance between the fault
685 and the surface, but neglects the shape of the topographic surface (Williams and Wadge, 2000).
686 It was previously known that the REC fails when topographic gradients are large (Williams and
687 Wadge, 2000), as they are in the Maule region. In this study, we additionally found that spatial
688 resolution of slip (largely controlled by data coverage) also plays a role in determining when the
689 REC will be effective. Using both synthetic tests and analysis of real events, we showed that the
690 REC only reduces a small fraction of the biases introduced by neglecting topography. The REC is
691 not sufficient even when those biases are limited, and when the data are uninformative, the REC
692 fails to recover any of the differences in the topographic model.

693 In conclusion, the effect of topography on static slip models is significant, and can only some-
694 times be accounted for using the receiver elevation correction. Our findings suggest that, in many
695 cases, it is advisable to use topographic Green's functions when inferring slip models in regions
696 with strong topographic gradients and/or poor observational constraints, such as in a subduction
697 zone. In regions with excellent data coverage (e.g. InSAR data with two different lines-of-sight)
698 and mild topographic variations, the REC may be used to account for topography.

699 *5.3. Perspectives*

700 Although the two examples of the Gorkha and Maule earthquakes represent two endmembers of
701 topography and data coverage, they are not sufficient for a complete understanding of the impact
702 of topography on static slip inversions because they both belong to the same class of earthquake
703 – namely, dip-slip events that occur close to the surface on shallowly dipping faults. Additional
704 research is needed to determine whether the results found in this work extend to other types of
705 earthquakes and faults. Does topography still have a significant effect when deformation is mostly
706 horizontal, as it is for a strike-slip fault? Furthermore, it seems intuitive that deeper earthquakes
707 would sense topography less. Is there a cut-off depth below which topography can be neglected?
708 What role, if any, does the dip of a fault play? How extreme must the topography of a region be for
709 the effect to start being considered significant? Topography may be short-wavelength (many small
710 structures) or long-wavelength (several large features); does the length scale of the topography
711 matter when determining whether it is likely to be impactful?

712 We must also remember that topography is only one aspect of 3D Earth structure. In this
713 study, we chose to focus on topography because the results of a previous study (Langer et al., 2019)

31

implied that it was likely to have the greatest impact on inferred slip models of the earthquakes that we analyzed in this study. Topography also has the advantage of being known everywhere with sufficient precision to be acknowledged a priori in a routine way. In comparison, fault geometry and elastic structure are only known for a few areas and events. Where these properties are poorly known, a good approach is to characterize the associated uncertainties and include them in the inverse problem (e.g., Minson et al., 2013; Duputel et al., 2014; Ragon et al., 2018, 2019b). These effects have been investigated by a few studies (see Section 1 for a thorough review), but since they can take many forms, their generic impact is not yet known. More research is needed before we can start to determine the trade-offs between these different contributions.

Finally, our conclusions are not restricted to coseismic deformation; topography may also affect estimates of postseismic stress relaxation, which is generally modeled by several interacting mechanisms, such as afterslip (e.g., Marone et al., 1991) or viscoelastic deformation in the lower crust or mantle (e.g., Pollitz et al., 1998; Perfettini and Avouac, 2004; Barbot and Fialko, 2010). Afterslip is of the same nature as coseismic deformation (slip on a fault surface) but of lower amplitude: it is thus constrained by less informative observations. The impact of topography on afterslip estimates is therefore probably even greater than for coseismic slip models. In contrast, viscoelastic deformation usually occurs at greater depths (e.g., Pollitz et al., 1998), so its estimates might be less influenced by topography.

Additionally, topography may affect images of interseismic slip rate deficit (or kinematic coupling ratio), which is usually modeled to decipher which portions of thrust faults are likely to rupture and which portions slip aseismically. A megathrust is usually coupled at intermediate to shallow depths (e.g. Stevens and Avouac, 2015; Xue et al., 2015; Métois et al., 2016; Michel et al., 2019). Almeida et al. (2018a) concluded that the coupling is generally underestimated in shallow regions, and thus where spatial resolution is low and topographic gradients are high. Yet, megathrust coupling is usually modeled using the homogeneous elastic half-space approximation (e.g. Chlieh et al., 2011; Loveless and Meade, 2016; Nocquet et al., 2017; Dal Zilio et al., 2020, and previous citations).

Incorporating 3D complexity would be more easily done if Green's functions with 3D structure, especially topography, could be calculated automatically by SPECFEM-X with minimal input from the user. The main barrier towards achieving this goal is that mesh generation is a complex process. High-quality topographic meshes are often difficult to construct, even with the simple requirements of SPECFEM-X, and each mesh must be fine-tuned by hand. However, we do plan to share the scripts required to produce the Green's functions used in this study on Github so that others may use them as a guide.

In summary, we showed that neglecting topography can lead to biased estimates of slip distribution on faults, especially in areas where topographic gradients are large. Accounting for topography, something which can now be done almost routinely with numerical tools such as SPECFEM-X, is thus an essential step towards achieving a reliable and detailed estimate of fault slip behavior (slip episodes or slip deficit) in region with large topographic variations.

The meshes used to calculate Green's functions in a topographic domain for the Gorkha and Maule earthquakes can be found in our repository (`doi:10.5281/zenodo.3675999`).

Acknowledgements

References

Almeida, R., Lindsey, E.O., Bradley, K., Hubbard, J., Mallick, R., Hill, E.M., 2018a. Can the Updip Limit of Frictional Locking on Megathrusts Be Detected Geodetically? Quantifying the Effect of Stress Shadows on Near-Trench Coupling. Geophysical Research Letters 45, 4754–4763. doi:10.1029/2018GL077785.

Almeida, R.V., Hubbard, J., Liberty, L., Foster, A., Sapkota, S.N., 2018b. Seismic imaging of the Main Frontal Thrust in Nepal reveals a shallow décollement and blind thrusting. Earth and Planetary Science Letters 494, 216–225. URL: http://www.sciencedirect.com/science/article/pii/S0012821X18302486.

Aster, R.C., Borchers, B., Thurber, C.H., 2005. Parameter Estimation and Inverse Problems. Academic Press.

Barbot, S., Fialko, Y., 2010. A unified continuum representation of post-seismic relaxation mechanisms: Semi-analytic models of afterslip, poroelastic rebound and viscoelastic flow. Geophysical Journal International 182, 1124–1140. doi:10.1111/j.1365-246X.2010.04678.x.

Beresnev, I.A., 2003. Uncertainties in Finite-Fault Slip Inversions: To What Extent to Believe? (A Critical Review). Bulletin of the Seismological Society of America 93, 2445–2458. doi:10.1785/0120020225.

Causse, M., Cotton, F., Mai, P.M., 2010. Constraining the roughness degree of slip heterogeneity. J. Geophys. Res. 115. doi:10.1029/2009jb006747.

Chlieh, M., Perfettini, H., Tavera, H., Avouac, J.P., Remy, D., Nocquet, J.M., Rolandone, F., Bondoux, F., Gabalda, G., Bonvalot, S., 2011. Interseismic coupling and seismic potential along the Central Andes subduction zone. Journal of Geophysical Research: Solid Earth 116. doi:10.1029/2010JB008166.

Comte, D., Eisenberg, A., Lorca, E., Pardo, M., Ponce, L., Saragoni, R., Singh, S.K., Suárez, G., 1986. The 1985 Central Chile Earthquake: A Repeat of Previous Great Earthquakes in the Region? Science 233, 449–453. doi:10.1126/science.233.4762.449.

Dahlen, F.A., Tromp, J., 1998. Theoretical Global Seismology. Princeton University Press.

Dal Zilio, L., Jolivet, R., van Dinther, Y., 2020. Segmentation of the main himalayan thrust illuminated by bayesian inference of interseismic coupling. Geophysical Research Letters

47, e2019GL086424. URL: https://agupubs.onlinelibrary.wiley.com/doi/abs/10.1029/2019GL086424, doi:10.1029/2019GL086424.

Delouis, B., Nocquet, J.M., Vallée, M., 2010. Slip distribution of the February 27, 2010 Mw = 8.8 Maule Earthquake, central Chile, from static and high-rate GPS, InSAR, and broadband teleseismic data. Geophysical Research Letters 37. doi:10.1029/2010GL043899.

Du, Y., Aydin, A., Segall, P., 1992. Comparison of various inversion techniques as applied to the determination of a geophysical deformation model for the 1983 Borah Peak earthquake. bssa 82, 1840–1866.

Duputel, Z., Agram, P.S., Simons, M., Minson, S.E., Beck, J.L., 2014. Accounting for prediction uncertainty when inferring subsurface fault slip. Geophysical Journal International 197, 464–482. doi:10.1093/gji/ggt517.

Elliott, J., Jolivet, R., González, P.J., Avouac, J.P., Hollingsworth, J., Searle, M.P., Stevens, V., 2016. Himalayan megathrust geometry and relation to topography revealed by the Gorkha earthquake. Nature Geoscience 9, 174–180. URL: https://doi.org/10.1038/ngeo2623.

Feng, G., Zhu, J., Li, Z., Zhang, G., Shan, X., Zhang, L., 2015. Geodetic model of the 2015 April 25 Mw 7.8 Gorkha Nepal Earthquake and Mw 7.3 aftershock estimated from InSAR and GPS data. Geophysical Journal International 203, 896–900. doi:10.1093/gji/ggv335.

Galetzka, J., Melgar, D., Genrich, J.F., Geng, J., Owen, S., Lindsey, E.O., Xu, X., Bock, Y., Avouac, J.P., Adhikari, L.B., Upreti, B.N., Pratt-Sitaula, B., Bhattarai, T.N., Sitaula, B.P., Moore, A., Hudnut, K.W., Szeliga, W., Normandeau, J., Fend, M., Flouzat, M., Bollinger, L., Shrestha, P., Koirala, B., Gautam, U., Bhatterai, M., Gupta, R., Kandel, T., Timsina, C., Sapkota, S.N., Rajaure, S., Maharjan, N., 2015. Slip pulse and resonance of the Kathmandu basin during the 2015 Gorkha earthquake, Nepal. Science 349, 1091–1095. URL: https://science.sciencemag.org/content/349/6252/1091, doi:10.1126/science.aac6383.

Gallovič, F., Imperatori, W., Mai, P.M., 2015. Effects of three-dimensional crustal structure and smoothing constraint on earthquake slip inversions: Case study of the Mw 6.3 2009 L'Aquila earthquake. Journal of Geophysical Research: Solid Earth 120, 428–449. doi:10.1002/2014JB011650.

Gharti, H.N., Langer, L., Tromp, J., 2019. Spectral-infinite-element simulations of coseismic and post-earthquake deformation. Geophysical Journal International 216, 1364–1393. URL: http://dx.doi.org/10.1093/gji/ggy495, doi:10.1093/gji/ggy495.

Gombert, B., Duputel, Z., Jolivet, R., Doubre, C., Rivera, L., Simons, M., 2017. Revisiting the 1992 Landers earthquake: a Bayesian exploration of co-seismic slip and off-fault damage. Geophysical Journal International 212, 839–852. doi:10.1093/gji/ggx455.

Grandin, R., Doin, M.P., Bollinger, L., Pinel-Puysségur, B., Ducret, G., Jolivet, R., Sapkota, S.N., 2012. Long-term growth of the Himalaya inferred from interseismic InSAR measurement. Geology 40, 1059–1062. URL: https://doi.org/10.1130/G33154.1, doi:10.1130/G33154.1.

Grandin, R., Vallée, M., Satriano, C., Lacassin, R., Klinger, Y., Simoes, M., Bollinger, L., 2015. Rupture process of the Mw=7.9 2015 Gorkha earthquake (Nepal): Insights into Himalayan megathrust segmentation. Geophysical Research Letters 42, 8373–8382. doi:10.1002/2015gl066044.

Hartzell, S., Liu, P., Mendoza, C., Ji, C., Larson, K.M., 2007. Stability and Uncertainty of Finite-Fault Slip Inversions: Application to the 2004 Parkfield, California, Earthquake. Bulletin of the Seismological Society of America 97, 1911–1934. doi:10.1785/0120070080.

Hayes, G.P., Moore, G.L., Portner, D.E., Hearne, M., Flamme, H., Furtney, M., Smoczyk, G.M., 2018. Slab2, a comprehensive subduction zone geometry model. Science 362, 58–61. doi:10.1126/science.aat4723.

Herman, F., Copeland, P., Avouac, J.P., Bollinger, L., Mahéo, G., Le Fort, P., Rai, S., Foster, D., Pêcher, A., Stüwe, K., Henry, P., 2010. Exhumation, crustal deformation, and thermal structure of the Nepal Himalaya derived from the inversion of thermochronological and thermobarometric data and modeling of the topography. Journal of Geophysical Research: Solid Earth 115. URL: https://agupubs.onlinelibrary.wiley.com/doi/abs/10.1029/2008JB006126, doi:10.1029/2008JB006126.

Hsu, Y.J., Simons, M., Williams, C., Casarotti, E., 2011. Three-dimensional FEM derived elastic Green's functions for the coseismic deformation of the 2005 Mw 8.7 Nias-Simeulue, Sumatra earthquake. Geochemistry, Geophysics, Geosystems 12. URL: https://agupubs.onlinelibrary.wiley.com/doi/abs/10.1029/2011GC003553, doi:10.1029/2011GC003553, arXiv:https://agupubs.onlinelibrary.wiley.com/doi/pdf/10.1029/2011GC003553.

Huang, B.S., Yeh, Y.T., 1997. Effect of Near-fault Terrain upon Dislocation Modeling. pure and applied geophysics 150, 1–18. doi:10.1007/s000240050060.

Ingleby, T., Wright, T.J., Hooper, A., Craig, T.J., Elliott, J.R., 2020. Constraints on the Geometry and Frictional Properties of the Main Himalayan Thrust Using Coseismic, Postseismic,

and Interseismic Deformation in Nepal. Journal of Geophysical Research: Solid Earth 125, e2019JB019201. doi:10.1029/2019JB019201.

Jolivet, R., Duputel, Z., Riel, B., Simons, M., Rivera, L., Minson, S.E., Zhang, H., Aivazis, M.a.G., Ayoub, F., Leprince, S., Samsonov, S., Motagh, M., Fielding, E.J., 2014. The 2013 Mw 7.7 Balochistan Earthquake: Seismic Potential of an Accretionary Wedge. Bulletin of the Seismological Society of America 104, 1020–1030. doi:10.1785/0120130313.

Jolivet, R., Lasserre, C., Doin, M.P., Guillaso, S., Peltzer, G., Dailu, R., Sun, J., Shen, Z.K., Xu, X., 2012. Shallow creep on the Haiyuan fault (Gansu, China) revealed by SAR interferometry. Journal of Geophysical Research: Solid Earth 117. URL: https://agupubs.onlinelibrary. wiley.com/doi/abs/10.1029/2011JB008732, doi:10.1029/2011JB008732.

Koper, K.D., Hutko, A.R., Lay, T., Sufri, O., 2012. Imaging short-period seismic radiation from the 27 February 2010 Chile (MW 8.8) earthquake by back-projection of P, PP, and PKIKP waves. Journal of Geophysical Research: Solid Earth 117. doi:10.1029/2011JB008576.

Kyriakopoulos, C., Masterlark, T., Stramondo, S., Chini, M., Bignami, C., 2013. Coseismic slip distribution for the Mw 9 2011 Tohoku-Oki earthquake derived from 3-D FE modeling. Journal of Geophysical Research: Solid Earth 118, 3837–3847. URL: https://agupubs. onlinelibrary.wiley.com/doi/abs/10.1002/jgrb.50265, doi:10.1002/jgrb.50265, arXiv:https://agupubs.onlinelibrary.wiley.com/doi/pdf/10.1002/jgrb.50265.

Langer, L., Gharti, H.N., Tromp, J., 2019. Impact of topography and three-dimensional heterogeneity on coseismic deformation. Geophysical Journal International 217, 866–878. doi:10.1093/gji/ggz060.

Lay, T., 2011. A Chilean surprise. Nature 471, 174–175. doi:10.1038/471174a.

Lay, T., Ammon, C.J., Kanamori, H., Koper, K.D., Sufri, O., Hutko, A.R., 2010. Teleseismic inversion for rupture process of the 27 February 2010 Chile (Mw 8.8) earthquake. Geophysical Research Letters 37. doi:10.1029/2010GL043379.

Lin, Y.n.N., Sladen, A., Ortega-Culaciati, F., Simons, M., Avouac, J.P., Fielding, E.J., Brooks, B.A., Bevis, M., Genrich, J., Rietbrock, A., Vigny, C., Smalley, R., Socquet, A., 2013. Coseismic and postseismic slip associated with the 2010 Maule Earthquake, Chile: Characterizing the Arauco Peninsula barrier effect. Journal of Geophysical Research: Solid Earth 118, 3142–3159. doi:10.1002/jgrb.50207.

Lindsey, E.O., Natsuaki, R., Xu, X., Shimada, M., Hashimoto, M., Melgar, D., Sandwell, D.T., 2015. Line-of-sight displacement from ALOS-2 interferometry: Mw 7.8 Gorkha earthquake and Mw 7.3 aftershock. Geophysical Research Letters 42, 6655–6661. doi:`10.1002/2015gl065385`.

Liu, W., Yao, H., 2018. A New Strategy of Finite-Fault Inversion Using Multiscale Waveforms and Its Application to the 2015 Gorkha, Nepal, Earthquake. Bulletin of the Seismological Society of America 108, 1947–1961. URL: `https://doi.org/10.1785/0120170309`, doi:`10.1785/0120170309`.

Lohman, R.B., Simons, M., 2005. Some thoughts on the use of InSAR data to constrain models of surface deformation: Noise structure and data downsampling. Geochemistry, Geophysics, Geosystems 6. URL: `https://agupubs.onlinelibrary.wiley.com/doi/abs/10.1029/2004GC000841`, doi:`10.1029/2004GC000841`.

Loveless, J.P., Meade, B.J., 2016. Two decades of spatiotemporal variations in subduction zone coupling offshore Japan. Earth and Planetary Science Letters 436, 19–30. doi:`10.1016/j.epsl.2015.12.033`.

Madariaga, R., Métois, M., Vigny, C., Campos, J., 2010. Central Chile Finally Breaks. Science 328, 181–182. doi:`10.1126/science.1189197`.

Maksymowicz, A., Chadwell, C., Ruiz, J., Tréhu, A., Contreras-Reyes, E., Weinrebe, W., Díaz-Naveas, J., Gibson, J., Lonsdale, P., Tryon, M., 2017. Coseismic seafloor deformation in the trench region during the mw8. 8 maule megathrust earthquake. Scientific reports 7, 1–8.

Mansinha, L.a., Smylie, D., 1971. The displacement fields of inclined faults. Bulletin of the Seismological Society of America 61, 1433–1440.

Marone, C.J., Scholtz, C.H., Bilham, R., 1991. On the mechanics of earthquake afterslip. Journal of Geophysical Research: Solid Earth 96, 8441–8452. doi:`10.1029/91JB00275`.

Masterlark, T., 2003. Finite element model predictions of static deformation from dislocation sources in a subduction zone: Sensitivities to homogeneous, isotropic, Poisson-solid, and half-space assumptions. Journal of Geophysical Research: Solid Earth 108. doi:`10.1029/2002JB002296`.

McTigue, D.F., Segall, P., 1988. Displacements and tilts from dip-slip faults and magma chambers beneath irregular surface topography. Geophysical Research Letters 15, 601–604. doi:`10.1029/GL015i006p00601`.

Mendoza, M.M., Ghosh, A., Karplus, M.S., Klemperer, S.L., Sapkota, S.N., Adhikari, L.B., Velasco, A., 2019. Duplex in the Main Himalayan Thrust illuminated by aftershocks of the 2015 Mw 7.8 Gorkha earthquake. Nature Geoscience URL: `https://doi.org/10.1038/s41561-019-0474-8`.

Menke, W., 2012. Geophysical Data Analysis: Discrete Inverse Theory. Academic press.

Métois, M., Vigny, C., Socquet, A., 2016. Interseismic Coupling, Megathrust Earthquakes and Seismic Swarms Along the Chilean Subduction Zone (38–18S). Pure and Applied Geophysics 173, 1431–1449. doi:`10.1007/s00024-016-1280-5`.

Michel, S., Gualandi, A., Avouac, J.P., 2019. Interseismic Coupling and Slow Slip Events on the Cascadia Megathrust. Pure and Applied Geophysics 176, 3867–3891. doi:`10.1007/s00024-018-1991-x`.

Minson, S.E., Simons, M., Beck, J.L., 2013. Bayesian inversion for finite fault earthquake source models I—theory and algorithm. Geophysical Journal International 194, 1701–1726. doi:`10.1093/gji/ggt180`.

Moreno, M., Melnick, D., Rosenau, M., Baez, J., Klotz, J., Oncken, O., Tassara, A., Chen, J., Bataille, K., Bevis, M., Socquet, A., Bolte, J., Vigny, C., Brooks, B., Ryder, I., Grund, V., Smalley, B., Carrizo, D., Bartsch, M., Hase, H., 2012. Toward understanding tectonic control on the Mw 8.8 2010 Maule Chile earthquake. Earth and Planetary Science Letters 321–322, 152–165. doi:`10.1016/j.epsl.2012.01.006`.

Nishenko, S.P., 1991. Circum-Pacific Seismic Potential: 1989–1999, in: Okal, E.A. (Ed.), Aspects of Pacific Seismicity. Birkhäuser, Basel. Pageoph Topical Volumes, pp. 169–259. doi:`10.1007/978-3-0348-5639-3_2`.

Nocquet, J.M., Jarrin, P., Vallée, M., Mothes, P.A., Grandin, R., Rolandone, F., Delouis, B., Yepes, H., Font, Y., Fuentes, D., Régnier, M., Laurendeau, A., Cisneros, D., Hernandez, S., Sladen, A., Singaucho, J.C., Mora, H., Gomez, J., Montes, L., Charvis, P., 2017. Supercycle at the Ecuadorian subduction zone revealed after the 2016 Pedernales earthquake. Nature Geoscience 10, 145–149. doi:`10.1038/ngeo2864`.

Nábělek, J., Hetényi, G., Vergne, J., Sapkota, S., Kafle, B., Jiang, M., Su, H., Chen, J., Huang, B.S., Team, t.H.C.L.I.M.B., 2009. Underplating in the Himalaya-Tibet collision zone revealed by the Hi-CLIMB experiment. Science 325, 1371–1374. URL: `http://science.sciencemag.org/content/325/5946/1371.abstract`.

Okada, Y., 1992. Internal deformation due to shear and tensile faults in a half-space. Bulletin of the Seismological Society of America 82, 1018–1040.

Perfettini, H., Avouac, J.P., 2004. Postseismic relaxation driven by brittle creep: A possible mechanism to reconcile geodetic measurements and the decay rate of aftershocks, application to the Chi-Chi earthquake, Taiwan. Journal of Geophysical Research: Solid Earth 109, B02304. doi:10.1029/2003JB002488.

Pollitz, F., Brooks Ben, Tong Xiaopeng, Bevis Michael G., Foster James H., Bürgmann Roland, Smalley Robert, Vigny Christophe, Socquet Anne, Ruegg Jean-Claude, Campos Jaime, Barrientos Sergio, Parra Héctor, Soto Juan Carlos Baez, Cimbaro Sergio, Blanco Mauro, 2011. Coseismic slip distribution of the February 27, 2010 Mw 8.8 Maule, Chile earthquake. Geophysical Research Letters 38. doi:10.1029/2011GL047065.

Pollitz, F.F., Bürgmann, R., Segall, P., 1998. Joint estimation of afterslip rate and postseismic relaxation following the 1989 Loma Prieta earthquake. Journal of Geophysical Research: Solid Earth 103, 26975–26992. doi:10.1029/98JB01554.

Ragon, T., Sladen, A., Bletery, Q., Vergnolle, M., Cavalié, O., Avallone, A., Balestra, J., Delouis, B., 2019a. Joint Inversion of Coseismic and Early Postseismic Slip to Optimize the Information Content in Geodetic Data: Application to the 2009 Mw6.3 L'Aquila Earthquake, Central Italy. Journal of Geophysical Research: Solid Earth doi:10.1029/2018JB017053.

Ragon, T., Sladen, A., Simons, M., 2018. Accounting for uncertain fault geometry in earthquake source inversions – I: theory and simplified application. Geophysical Journal International 214, 1174–1190. doi:10.1093/gji/ggy187.

Ragon, T., Sladen, A., Simons, M., 2019b. Accounting for uncertain fault geometry in earthquake source inversions – II: Application to the Mw 6.2 Amatrice earthquake, Central Italy. Geophysical Journal International doi:10.1093/gji/ggz180.

Ruegg, J.C., Rudloff, A., Vigny, C., Madariaga, R., de Chabalier, J.B., Campos, J., Kausel, E., Barrientos, S., Dimitrov, D., 2009. Interseismic strain accumulation measured by GPS in the seismic gap between Constitución and Concepción in Chile. Physics of the Earth and Planetary Interiors 175, 78–85. doi:10.1016/j.pepi.2008.02.015.

Ruiz, S., Madariaga, R., Astroza, M., Saragoni, G.R., Lancieri, M., Vigny, C., Campos, J., 2012. Short-Period Rupture Process of the 2010 Mw 8.8 Maule Earthquake in Chile. Earthquake Spectra 28, S1–S18. doi:10.1193/1.4000039.

Sladen, A., Trevisan, J., 2018. Shallow megathrust earthquake ruptures betrayed by their outer-trench aftershocks signature. Earth and Planetary Science Letters 483, 105–113.

Steketee, J., 1958. On volterra's dislocations in a semi-infinite elastic medium. Canadian Journal of Physics 36, 192–205.

Stevens, V.L., Avouac, J.P., 2015. Interseismic coupling on the main Himalayan thrust. Geophysical Research Letters 42, 5828–5837. doi:`10.1002/2015GL064845`.

Tinti, S., Armigliato, A., 2002. A 2-D hybrid technique to model the effect of topography on coseismic displacements. Application to the Umbria-Marche (central Italy) 1997 earthquake sequence. Geophysical Journal International 150, 542–557. doi:`10.1046/j.1365-246X.2002.01721.x`.

Tong, X., Sandwell, D., Luttrell, K., Brooks, B., Bevis, M., Shimada, M., Foster, J., Smalley, R., Parra, H., Soto, J.C.B., Blanco, M., Kendrick, E., Genrich, J., Caccamise, D.J., 2010. The 2010 Maule, Chile earthquake: Downdip rupture limit revealed by space geodesy. Geophysical Research Letters 37. doi:`10.1029/2010GL045805`.

Trasatti, E., Kyriakopoulos, C., Chini, M., 2011. Finite element inversion of DInSAR data from the Mw 6.3 L'Aquila earthquake, 2009 (Italy). Geophysical Research Letters 38. URL: `https://agupubs.onlinelibrary.wiley.com/doi/abs/10.1029/2011GL046714`, doi:`10.1029/2011GL046714`.

Tsai, V.C., Ampuero, J.P., Kanamori, H., Stevenson, D.J., 2013. Estimating the effect of Earth elasticity and variable water density on tsunami speeds. Geophysical Research Letters 40, 492–496. doi:`10.1002/grl.50147`.

Tung, S., Masterlark, T., 2016. Coseismic slip distribution of the 2015 Mw7.8 Gorkha, Nepal, earthquake from joint inversion of GPS and InSAR data for slip within a 3-D heterogeneous domain. Journal of Geophysical Research: Solid Earth 121, 3479–3503. URL: `https://agupubs.onlinelibrary.wiley.com/doi/abs/10.1002/2015JB012497`, doi:`10.1002/2015JB012497`.

Twardzik, C., Vergnolle, M., Sladen, A., Avallone, A., 2019. Unravelling the contribution of early postseismic deformation using sub-daily GNSS positioning. Scientific Reports 9, 1775. doi:`10.1038/s41598-019-39038-z`.

Vigny, C., Socquet, A., Peyrat, S., Ruegg, J.C., Métois, M., Madariaga, R., Morvan, S., Lancieri, M., Lacassin, R., Campos, J., Carrizo, D., Bejar-Pizarro, M., Barrientos, S., Armijo, R., Aranda,

C., Valderas-Bermejo, M.C., Ortega, I., Bondoux, F., Baize, S., Lyon-Caen, H., Pavez, A., Vilotte, J.P., Bevis, M., Brooks, B., Smalley, R., Parra, H., Baez, J.C., Blanco, M., Cimbaro, S., Kendrick, E., 2011. The 2010 Mw 8.8 Maule Megathrust Earthquake of Central Chile, Monitored by GPS. Science 332, 1417–1421. doi:`10.1126/science.1204132`.

Wang, K., Fialko, Y., 2015. Slip model of the 2015 Mw 7.8 Gorkha (Nepal) earthquake from inversions of ALOS-2 and GPS data. Geophysical Research Letters 42, 7452–7458. URL: `https://agupubs.onlinelibrary.wiley.com/doi/abs/10.1002/2015GL065201`, doi:`10.1002/2015GL065201`, arXiv:`https://agupubs.onlinelibrary.wiley.com/doi/pdf/10.1002/2015GL065201`.

Wang, K., Fialko, Y., 2018. Observations and modeling of coseismic and postseismic deformation due to the 2015 Mw 7.8 Gorkha (Nepal) earthquake. Journal of Geophysical Research: Solid Earth 123, 761–779. URL: `https://agupubs.onlinelibrary.wiley.com/doi/abs/10.1002/2017JB014620`, doi:`10.1002/2017JB014620`, arXiv:`https://agupubs.onlinelibrary.wiley.com/doi/pdf/10.1002/2017JB014620`.

Wang, X., Wei, S., Wu, W., 2017. Double-ramp on the Main Himalayan Thrust revealed by broadband waveform modeling of the 2015 Gorkha earthquake sequence. Earth and Planetary Science Letters 473, 83–93. URL: `http://www.sciencedirect.com/science/article/pii/S0012821X1730300X`.

Watada, S., Kusumoto, S., Satake, K., 2014. Traveltime delay and initial phase reversal of distant tsunamis coupled with the self-gravitating elastic Earth. Journal of Geophysical Research: Solid Earth 119, 4287–4310. doi:`10.1002/2013JB010841`.

Wessel, P., Luis, J.F., Uieda, L., Scharroo, R., Wobbe, F., Smith, W.H.F., Tian, D., 2019. The Generic Mapping Tools Version 6. Geochemistry, Geophysics, Geosystems n/a. doi:`10.1029/2019GC008515`.

Whipple, K.X., Shirzaei, M., Hodges, K.V., Ramon Arrowsmith, J., 2016. Active shortening within the Himalayan orogenic wedge implied by the 2015 Gorkha earthquake. Nature Geoscience 9, 711–716. URL: `https://doi.org/10.1038/ngeo2797`.

Williams, C.A., Wadge, G., 1998. The effects of topography on magma chamber deformation models: Application to Mt. Etna and radar interferometry. Geophysical Research Letters 25, 1549–1552. doi:`10.1029/98GL01136`.

Williams, C.A., Wadge, G., 2000. An accurate and efficient method for including the effects of topography in three-dimensional elastic models of ground deformation with applications to radar interferometry. Journal of Geophysical Research: Solid Earth 105, 8103–8120. URL: `https://agupubs.onlinelibrary.wiley.com/doi/abs/10.1029/1999JB900307`, doi:`10.1029/1999JB900307`, arXiv:`https://agupubs.onlinelibrary.wiley.com/doi/pdf/10.1029/1999JB900307`.

Williams, C.A., Wallace, L.M., 2018. The Impact of Realistic Elastic Properties on Inversions of Shallow Subduction Interface Slow Slip Events Using Seafloor Geodetic Data. Geophysical Research Letters 45, 7462–7470. doi:`10.1029/2018GL078042`.

Xue, L., Schwartz, S., Liu, Z., Feng, L., 2015. Interseismic megathrust coupling beneath the Nicoya Peninsula, Costa Rica, from the joint inversion of InSAR and GPS data. Journal of Geophysical Research: Solid Earth 120, 3707–3722. doi:`10.1002/2014JB011844`.

Yadav, R.K., Roy, P.N.S., Gupta, S.K., Khan, P.K., Catherine, J.K., Prajapati, S.K., Kumar, A., Puviarasan, N., Bhu, H., Devachandra, M., Malik, J., Kundu, B., Debbarma, C., Gahalaut, V.K., 2017. Rupture model of Mw 7.8 2015 Gorkha, Nepal earthquake: Constraints from GPS measurements of coseismic offsets. Journal of Asian Earth Sciences 133, 56–61. URL: `http://www.sciencedirect.com/science/article/pii/S136791201630092X`.

Yagi, Y., Okuwaki, R., 2015. Integrated seismic source model of the 2015 Gorkha, Nepal, earthquake. Geophysical Research Letters 42, 6229–6235. URL: `https://agupubs.onlinelibrary.wiley.com/doi/abs/10.1002/2015GL064995`, doi:`10.1002/2015GL064995`.

Yang, Y., Chen, Q., Xu, Q., Liu, G., Hu, J.C., 2019. Source model and coulomb stress change of the 2015 Mw 7.8 Gorkha earthquake determined from improved inversion of geodetic surface deformation observations. Journal of Geodesy 93, 333–351. URL: `https://doi.org/10.1007/s00190-018-1164-9`.

Yi, L., Xu, C., Zhang, X., Wen, Y., Jiang, G., Li, M., Wang, Y., 2017. Joint inversion of GPS, InSAR and teleseismic data sets for the rupture process of the 2015 Gorkha, Nepal, earthquake using a generalized ABIC method. Journal of Asian Earth Sciences 148, 121–130. URL: `http://www.sciencedirect.com/science/article/pii/S1367912017304601`.

Yoshimoto, M., Watada, S., Fujii, Y., Satake, K., 2016. Source estimate and tsunami forecast from far-field deep-ocean tsunami waveforms—The 27 February 2010 Mw 8.8 Maule earthquake. Geophysical Research Letters 43, 659–665. doi:`10.1002/2015GL067181`.

Yue, H., Lay, T., Rivera, L., An, C., Vigny, C., Tong, X., Soto, J.C.B., 2014. Localized fault slip to the trench in the 2010 Maule, Chile Mw = 8.8 earthquake from joint inversion of high-rate GPS, teleseismic body waves, InSAR, campaign GPS, and tsunami observations. Journal of Geophysical Research: Solid Earth 119, 7786–7804. doi:`10.1002/2014JB011340`.

Yue, H., Simons, M., Duputel, Z., Jiang, J., Fielding, E., Liang, C., Owen, S., Moore, A., Riel, B., Ampuero, J.P., Samsonov, S.V., 2017. Depth varying rupture properties during the 2015 Mw 7.8 Gorkha (Nepal) earthquake. Special Issue on the 25 April 2015 Mw 7.8 Gorkha (Nepal) Earthquake 714-715, 44–54. URL: `http://www.sciencedirect.com/science/article/pii/S0040195116302566`.

Zhao, S., Kaneda, Y., Müller, R.D., Takahashi, Y., 2004. 3-D finite-element modelling of deformation and stress associated with faulting: effect of inhomogeneous crustal structures. gji 157, 629–644. URL: `https://dx.doi.org/10.1111/j.1365-246X.2004.02200.x`.

Zuo, R., Qu, C., Shan, X., Zhang, G., Song, X., 2016. Coseismic deformation fields and a fault slip model for the Mw7.8 mainshock and Mw7.3 aftershock of the Gorkha-Nepal 2015 earthquake derived from Sentinel-1A SAR interferometry. Tectonophysics 686, 158–169. URL: `http://www.sciencedirect.com/science/article/pii/S0040195116303146`.